Structural and Multidisciplinary Optimization (2022) 65:110
https://doi.org/10.1007/s00158-022-03198-w

RESEARCH PAPER

Design optimization and sensitivity analysis on time-domain sound radiation of laminated curved shell structures

Hao Zheng[1] · Yang Yu[2] · Guozhong Zhao[1] · Tianzeng Tao[1] · Bowei Huang[1] · Yu Guo[1]

Received: 5 April 2021 / Revised: 16 December 2021 / Accepted: 11 February 2022 / Published online: 9 March 2022

Abstract

Compared with the frequency-domain sound radiation analysis, the time-domain analysis is more suitable for complicated engineering problems. However, the research on design optimization of time-domain sound radiation was rarely reported. To reduce the undesired time-domain noise radiated from laminated curved shells, the sensitivity formulation of transient sound pressure is obtained by directly differentiating response equations and the corresponding optimization procedure is presented. The Newmark integral method is applied to calculate the vibration response, and the results of which are input into the sound radiation analysis as boundary conditions. Combined with the time-domain boundary element method (BEM), the time-domain boundary integral equation is numerically discretized in both the spatial and time domains, and the transient sound pressure is obtained by solving an algebraic equation. To reduce the time-domain noise, ply thicknesses are taken as the design variables to minimize the square of sound pressure on a prescribed reference surface in the sound medium or the structural surface over a certain period of time. In addition, the constraint on the structural mass is considered. The calculation of time-domain sound radiation sensitivity is transformed into the following two processes: (a) the derivation of transient vibration response based on finite element method (FEM); (b) the derivation of transient sound pressure based on time-domain BEM. The optimal solution is obtained by using the method of moving asymptotes (MMA). Numerical examples verify the accuracy of the sensitivity formulae, and show that the time-domain sound radiation is significantly reduced within allowable constraints.

Keywords Laminated curved shells · Time-domain sound radiation · Sensitivity analysis · Design optimization · Ply thickness

1 Introduction

Laminated curved shells are widely used in aerospace engineering, transportation engineering and other fields due to their excellent performance. However, in some complex and dynamic environments, shell structures are often subject to transient loads, making such shell structures prone to generate undesired time-domain sound radiation, which further endangers the health of residents or damages delicate instruments. The sound radiation noise has gradually become a kind of environmental pollution which cannot be ignored. Therefore, it is of great significance for producers to reduce the time-domain noise radiated from laminated curved shell structures.

At present, many theoretical studies about the sound radiation of plates and shells have been made. However, when dealing with complex boundary conditions or geometrical shapes in practical engineering, sound radiation can only be calculated by using numerical methods such as FEM (Assaad et al. 1993; Chai et al. 2018), infinite element method (IFEM) (Zienkiewicz et al. 1985; Burnett 1994), BEM, etc. The BEM automatically satisfies the Sommerfeld radiation condition, wherein only the finite boundaries of vibrational structures need to be meshed. Thus, BEM is very suitable for external sound problems. Kim and Ih (2002)

Responsible Editor: Palaniappan Ramu

✉ Guozhong Zhao
zhaogz@dlut.edu.cn

[1] State Key Laboratory of Structural Analysis for Industrial Equipment, Department of Engineering Mechanics, Dalian University of Technology, Dalian 116024, People's Republic of China

[2] School of Locomotive and Rolling Stock Engineering, Dalian Jiaotong University, Dalian 116028, People's Republic of China

adopted a simplified BEM to solve high-frequency sound radiation problems. Considering the reflection and absorption of seabed, Zhang et al. (2020) calculated the sound pressure level of shells in shallow sea. The sound transmission problems of a fluid–structure coupled system were studied by Tong et al. (2007) using a direct-BEM/FEM. In addition, the effects of various parameters such as the support condition and lamination scheme, on sound radiation were studied by Sharma et al. (2018); the authors (Sharma et al. 2019) also investigated the acoustic responses of composite plates in an elevated thermal environment. Moreover, to reduce the computational effort, some improved methods based on BEM have been proposed (Chen et al. 2008; Li and Lian 2020).

However, most of research focuses on the frequency-domain analysis of steady-state sound problems based on the Helmholtz equation. In reality, lots of transient loads are often encountered in the fields of aerospace and transportation engineering, such as the braking of brake pads and the process of starting engines. Therefore, the frequency-domain analysis under harmonic excitations cannot meet the engineering requirements. Compared with the frequency-domain analysis, there have been few studies about the time-domain analysis of transient sound problems due to its complexity. The solution of time-domain boundary integral equation based on the wave equation is an effective approach to predict the time-domain sound radiation, and the quantities in sound field are calculated directly in the time domain. At present, the commonly used forms of the time-domain boundary integral equation mainly include the Kirchhoff integral equation and the formula derived by Mansur (1983). The two integral forms are completely equivalent. The Kirchhoff integral equation was discretized in both the time and spatial domains to calculate the transient sound radiation (Ebenezer and Stepanishen 1991). Qu et al. (2019a) calculated the time-domain sound pressure of composite plates affected by moving loads; the authors (Qu et al. 2019b) further investigated nonlinear time-domain vibro-acoustic behaviors of structures. The effects of boundary conditions (Ou and Mak 2011) and locations of stiffeners (Ou and Mak 2012) on the time-domain sound radiation have been studied. In addition, Tian et al. (2019) proposed a sound radiation calculation method based on modal expansion and spatial delay, which greatly improved the calculation efficiency compared with the traditional BEM.

The analysis of sound radiation characteristics is the basis of structural noise reduction. Researchers are more concerned about reducing noise by optimizing structural parameters. At present, intelligent optimization algorithms and mathematical programming algorithms based on gradient information are mainly used in the research. Some researchers used a simulated annealing algorithm (SA) to minimize sound radiation (Zhai et al. 2017, 2020). Jeon and Okuma (2008) adopted a particle swarm optimization algorithm (PSOA) to optimize the embossed panel to reduce sound power. To obtain the global optimal value, Joshi et al. (2010) combined a PSOA and a modified method of feasible directions to minimize sound radiation. In addition, a multi-islands genetic algorithm was employed to reduce sound power (Yang et al. 2016). However, exorbitant computation cost is the biggest disadvantage of intelligent algorithms in dealing with optimization problems, especially for the sound field problems with large computational efforts. The sensitivity information reflects the sensitivity degrees of the optimization indexes with respect to structural parameters and provides the best search direction for design optimization. For this reason, mathematical programming algorithms are widely used in the design optimization of sound radiation problems due to their high computing efficiency. Lamancusa and Eschenauer (1994) reduced sound power by optimizing the thickness and mass distributions of plates, but finite difference method (FDM) was used to derive the sensitivity information, resulting in a large amount of calculation. The noise radiation of a sandwich structure with cellular cores was reduced by optimizing the core shape (Denli and Sun 2007). The sound radiation of a composite board was minimized by Niu et al. (2010) using the Discrete Material Optimization (DMO) method. Yang and Li (2015) minimized the sound power at resonant frequencies of a bi-material plate in the thermal environment. Zhang et al. (2018) used evolutionary structural optimization (ESO) to obtain the optimal damping material layouts of a cavity structure. In addition, sound power and sound pressure radiated from vibrating structures were minimized by Du and Olhoff (2007, 2010) using topology optimization, respectively. Zheng et al. (2016) minimized the sound radiation at low frequency resonance of a plate by optimizing passive constrained layer damping. Zhao et al. (2018) reduced the sound power level of a shell by optimizing bi-material distribution. Ma and Cheng (2019) optimized damping layouts to minimize the sound radiation of an acoustic black hole plate. Besides, some researchers reduced sound radiation of a vibrating structure using microstructural topology optimization (Du and Yang 2015) or multi-scale topology optimization (Liang and Du 2019). In addition, Zhao et al. (2017) proposed a topology optimization approach based on the BEM and the optimality criteria (OC) method to reduce sound pressure. Many scholars have studied the sound field of flat shells. In reality, however, curved shells are often encountered in practical situations. Therefore, to meet practical needs, the sound radiation and structural optimization of curved shells has begun to emerge (Zhai et al. 2017; Sharma et al. 2019).

In addition, it is well known that sensitivity is a necessary condition to obtain optimal designs by using gradient algorithms. The FDM is described as the simplest method (Martins and Hwang 2013) to implement for calculating sensitivity, such as a forward FDM (De Leon et al. 2012; Pereyra et al. 2014). In FDM, sensitivity is determined by taking the difference between the perturbed and original values and then dividing by the perturbation step size. The detailed formulae can be found in (Lee and Park 1997; Li and Zheng 2017; Wang et al. 2018). Some scholars have also carried out further studies on FDM. For example, Gill et al. (1983) presented an algorithm to compute a set of intervals to be used in a forward difference approximation of the gradient. Nonetheless, the exorbitant calculation cost and uncertainty in the choice of a perturbation step size sometimes make this approach inapplicable. Therefore, FDM is commonly used for sensitivity verification at present, such as (Zhang and Kang 2014). In addition, Wang and Apte (2006) proposed a complex variable method without difference for eliminating condition error. Compared with FDM, this method is much less sensitive to step size. Furthermore, analytical approaches of sensitivity include the direct method and the adjoint variable method (Adelman and Haftka 1986). When the direct method is applied, both sides of the discrete equation are directly differentiated, and then the same numerical methods used to solve for responses are employed to calculate response sensitivities. Finally, the sensitivity information of objective functions can be further obtained by using the chain rule (Keulen et al. 2005). The adjoint variable method (Lee 1999) defines an adjoint problem which is independent of design variables, and then sensitivities of objective functions can be solved by using the structural and adjoint responses. Both the direct and adjoint variable methods contain fewer computational burdens than FDM, which needs to decompose the stiffness matrix per perturbation calculation, whereas the direct and adjoint variable methods merely require once factorization. When the number of design variables is more than the number of performance measures, the adjoint variable method is more efficient; on the contrary, the direct method is more efficient. Besides, the sensitivity analysis approach that combines the analytical methods and finite difference approximations is denoted as semi-analytical method. As mentioned in (Fernandez and Tortorelli 2018), the semi-analytical method shares the simplicity of the FDM and the efficiency of the analytical methods. Thus, this method still reduces the computational burden well. In addition, the computational or automatic differentiation is also studied by researchers (Keulen et al. 2005). So far, the research on sensitivity analysis in the structural-acoustics field has mainly addressed frequency-domain problems (Denli and Sun 2007; Niu et al. 2010; Liang and Du 2019), while the sensitivity analysis of time-domain sound radiation has not been investigated.

Notably, all of the above articles focus on the frequency domain. Due to the complexity and large amounts of calculation, there is no report on structural design optimization of time-domain sound radiation from vibrating laminated curved shells. Nonetheless, laminated curved shells and transient vibrations are among the most common structural forms and mechanical behaviors which are encountered in practical applications, respectively. In addition, for laminated structures affected by transient loads, the ply thicknesses have a great influence on the sound radiation. Hence, it is highly valuable to study the parameter optimization of laminated curved shells to reduce time-domain sound radiation.

To sum up, based on the sensitivity information, the time-domain sound radiation of laminated curved shells is reduced by optimizing structural ply thicknesses in this paper. The material of the paper is organized as follows. In Sect. 2, the Newmark integral method used to solve for transient vibration response is presented. In Sect. 3, the analysis and solution for the time-domain sound radiation are presented. Thus, in Sect. 3.1, the time-domain boundary integral equation is given, and this integral equation is numerically discretized in both the spatial and time domains in Sect. 3.2. In Sect. 4, the ply thickness optimization subject to a given mass constraint is formulated for problems of minimizing the square of sound pressure on a prescribed reference surface in the sound medium or the structural surface over a certain time period of interest. In Sect. 5, the sensitivity formulation of transient sound pressure with respect to ply thickness is obtained by directly differentiating response equations. Section 6.1 then verifies the accuracy of the sensitivity formulae, and Sect. 6.2 shows the effectiveness of the design optimization model by two examples, and Sect. 6.3 gives the computational performance of optimization examples. Section 7 concludes the paper.

2 Analysis for transient vibration response

In this paper, an eight-node laminated curved shell element is employed, and its finite element formulation is derived in Appendix 1. In addition, the dynamic equation of a shell structure affected by a transient load $\mathbf{F}(\mathbf{t})$ can be written as:

$$\mathbf{M}\ddot{\mathbf{u}} + \mathbf{C}\dot{\mathbf{u}} + \mathbf{K}\mathbf{u} = \mathbf{F}(\mathbf{t}) \tag{1}$$

where $\mathbf{M}$, $\mathbf{K}$ and $\mathbf{C}$ are the mass matrix, stiffness matrix and damping matrix, respectively; $\ddot{\mathbf{u}}$, $\dot{\mathbf{u}}$ and $\mathbf{u}$ are the acceleration, velocity and displacement vectors, respectively. Here, the Newmark integral method is applied to derive the discrete time-domain expressions for the dynamic equation. The equation of motion at time t_{n+1} is further depicted as

$$\mathbf{M}\ddot{\mathbf{u}}^{(n+1)} + \mathbf{C}\dot{\mathbf{u}}^{(n+1)} + \mathbf{K}\mathbf{u}^{(n+1)} = \mathbf{F}(\mathbf{t})^{(n+1)} \tag{2}$$

In the Newmark integral method, the nodal velocities, accelerations and displacements at times t_n and t_{n+1} satisfy the following equations:

$$\begin{aligned}\dot{\mathbf{u}}^{(n+1)} &= \dot{\mathbf{u}}^{(n)} + \left[(1-\delta)\ddot{\mathbf{u}}^{(n)} + \delta\ddot{\mathbf{u}}^{(n+1)}\right]\Delta t \\ \mathbf{u}^{(n+1)} &= \mathbf{u}^{(n)} + \dot{\mathbf{u}}^{(n)}\Delta t + \left[(0.5-\gamma)\ddot{\mathbf{u}}^{(n)} + \gamma\ddot{\mathbf{u}}^{(n+1)}\right](\Delta t)^2\end{aligned} \tag{3}$$

where Δt represents the time interval between two adjacent time points. When $\delta \geq 0.5$ and $\gamma \geq 0.25(0.5+\delta)^2$, the Newmark integral method is unconditionally stable. Therefore, all unknowns of the next time step can be iteratively calculated by using the values from the previous time step. Besides, the displacement $\mathbf{u}^{(n+1)}$ at time t_{n+1} can be solved by

$$\tilde{\mathbf{K}}\mathbf{u}^{(n+1)} = \tilde{\mathbf{F}}^{(n+1)} \tag{4}$$

with

$$\begin{aligned}\tilde{\mathbf{K}} &= \mathbf{K} + \psi_0\mathbf{M} + \psi_1\mathbf{C} \\ \tilde{\mathbf{F}}^{(n+1)} &= \mathbf{F}^{(n+1)} + \mathbf{F}_{\mathbf{M}} + \mathbf{F}_{\mathbf{C}} \\ \mathbf{F}_{\mathbf{M}} &= \mathbf{M}\left(\psi_0\mathbf{u}^{(n)} + \psi_2\dot{\mathbf{u}}^{(n)} + \psi_3\ddot{\mathbf{u}}^{(n)}\right) \\ \mathbf{F}_{\mathbf{C}} &= \mathbf{C}\left(\psi_1\mathbf{u}^{(n)} + \psi_4\dot{\mathbf{u}}^{(n)} + \psi_5\ddot{\mathbf{u}}^{(n)}\right)\end{aligned} \tag{5}$$

where $\tilde{\mathbf{K}}$ and $\tilde{\mathbf{F}}^{(n+1)}$ are the equivalent stiffness matrix and equivalent mechanical load vector at time t_{n+1}, respectively; $\psi_0 \sim \psi_5$ are constants, and their expressions can be found in (Taherifar et al. 2021).

3 Analysis and solution for time-domain sound radiation

Figure 1 shows a vibrational structure with a finite boundary and its exterior sound field with an infinite boundary. Here, $\mathbf{X}$ is a source point; $\mathbf{Y}$ is a field point; and $\mathbf{n}$ represents the outer normal direction of the structural boundary.

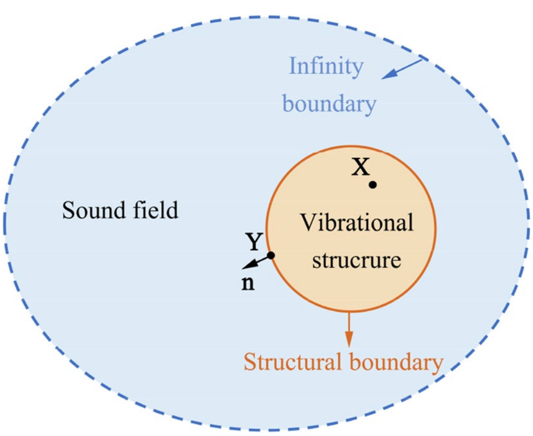

Fig. 1 Vibrational structure and exterior sound field

3.1 Time-domain boundary integral equation

The propagation of small amplitude sound waves through a homogeneous medium can be formulated as (Wu 2000):

$$\nabla^2 p(\mathbf{Y},t) - \frac{1}{c^2}\ddot{p}(\mathbf{Y},t) = -\chi(\mathbf{Z},t) \tag{6}$$

where ∇^2 is the Laplace operator; $p(\mathbf{Y},t)$ is the transient sound pressure of the field point $\mathbf{Y}$ at time t; $\ddot{p}$ is the second order derivative of the sound pressure with respect to time; c is the speed of sound propagation; and $\chi(\mathbf{Z},t)$ is a sound source. Under homogeneous initial conditions, i.e., $p(\mathbf{Y},0) = \partial p(\mathbf{Y},0)/\partial t = 0$, the general solution for this wave equation is given by:

$$p(\mathbf{Y},t) = \frac{1}{4\pi}\int_\Omega \frac{1}{r}\chi\left(\mathbf{Z}, t-\frac{r}{c}\right)\mathrm{d}\Omega(\mathbf{Z}) \tag{7}$$

where $r = |\mathbf{Y}-\mathbf{Z}|$. By substituting the sound source $\chi(\mathbf{Z},t) = \delta(t-\tau)\delta(\mathbf{Z}-\mathbf{X})$ into the general solution, the following fundamental solution is obtained:

$$p^*(\mathbf{Y},t;\mathbf{X},\tau) = \frac{1}{4\pi r}\delta\left(t-\frac{r}{c}-\tau\right) \tag{8}$$

where $r = |\mathbf{Y}-\mathbf{X}|$; δ is the Dirac delta function; and $p^*(\mathbf{Y},t;\mathbf{X},\tau)$ represents the response of the field point $\mathbf{Y}$ at time t due to an impulse at time τ located at the source point $\mathbf{X}$. By taking the derivative of this fundamental solution with respect to $\mathbf{n}$ as shown in Fig. 1, we further obtain the fundamental flux as follows.

$$\begin{aligned}q^*(\mathbf{Y},t;\mathbf{X},\tau) &= \frac{\partial p^*(\mathbf{Y},t;\mathbf{X},\tau)}{\partial \mathbf{n}} \\ &= -\frac{1}{4\pi r^2}\left[\delta\left(t-\frac{r}{c}-\tau\right) + \frac{r}{c}\dot{\delta}\left(t-\frac{r}{c}-\tau\right)\right]\frac{\partial r}{\partial \mathbf{n}}\end{aligned} \tag{9}$$

In addition, the Laplace transform and inverse transform can be employed to derive the following time-domain boundary integral equation without external sound sources under homogeneous initial conditions (Wu 2000):

$$\begin{aligned}&\Theta(\mathbf{Y})p(\mathbf{Y},t) + \int_\Gamma\int_0^t q^*(\mathbf{Y},t;\mathbf{X},\tau)p(\mathbf{X},\tau)\mathrm{d}\tau\mathrm{d}\Gamma \\ &= \int_\Gamma\int_0^t p^*(\mathbf{Y},t;\mathbf{X},\tau)q(\mathbf{X},\tau)\mathrm{d}\tau\mathrm{d}\Gamma\end{aligned} \tag{10}$$

where $\Theta(\mathbf{Y})$ is a constant that depends on the location of the field point $\mathbf{Y}$; $p(\mathbf{X},\tau)$ and $q(\mathbf{X},\tau)$ are the sound pressure and sound flux of the source point $\mathbf{X}$ at time τ, respectively; and the sound flux is associated with the vibration response through the following equation:

$$\mathbf{q} = -\rho_a\ddot{\mathbf{u}}_N \tag{11}$$

where $\mathbf{q}$ is the matrix containing the sound flux values of all boundary points at all time points; ρ_a is the density of air; and $\ddot{\mathbf{u}}_N$ is the structural normal acceleration matrix.

3.2 Solution for time-domain sound pressure

In this section, the transient sound pressure is obtained by solving an algebraic equation which is derived by numerically discretizing Eq. (10) in both the spatial and time domains. To solve for the sound pressure at time t_n, we assume that the time domain is uniformly divided into n time steps, and both the sound pressure and sound flux are linearly distributed at the mth time step. Hence, the values at time τ within the mth time step can be calculated through the following interpolation relationships:

$$\begin{aligned} p(\mathbf{X},\tau) &= \sum_{b=1}^{2} L^b p^{b(m)}(\mathbf{X}) \\ q(\mathbf{X},\tau) &= \sum_{b=1}^{2} L^b q^{b(m)}(\mathbf{X}) \end{aligned} \tag{12}$$

with

$$L^1 = \left(1-\frac{\tau}{\Delta t}\right),\ L^2 = \left(\frac{\tau}{\Delta t}\right) \tag{13}$$

where $p^{b(m)}$ and $q^{b(m)}$ are the sound pressure and sound flux at the bth time interpolation point belonging to the mth time step, respectively; L is the interpolation function; and Δt is the time interval between two time points. Substituting Eq. (12) into Eq. (10) yields:

$$\begin{aligned} &\Theta(\mathbf{Y})p\left(\mathbf{Y},t_n\right) + \int_\Gamma \sum_{m=1}^{n} \int_{t_{m-1}}^{t_m} q^*\left(\mathbf{Y},t_n;\mathbf{X},\tau\right) \sum_{b=1}^{2} L^b p^{b(m)}(\mathbf{X})\mathrm{d}\tau\mathrm{d}\Gamma \\ &= \int_\Gamma \sum_{m=1}^{n} \int_{t_{m-1}}^{t_m} p^*\left(\mathbf{Y},t_n;\mathbf{X},\tau\right) \sum_{b=1}^{2} L^b q^{b(m)}(\mathbf{X})\mathrm{d}\tau\mathrm{d}\Gamma \end{aligned} \tag{14}$$

Here, we set:

$$\begin{aligned} {}^{(b)}P^{(n)(m)}(\mathbf{Y};\mathbf{X}) &= \int_{t_{m-1}}^{t_m} p^*\left(\mathbf{Y},t_n;\mathbf{X},\tau\right)L^b\mathrm{d}\tau \\ {}^{(b)}Q^{(n)(m)}(\mathbf{Y};\mathbf{X}) &= \int_{t_{m-1}}^{t_m} q^*\left(\mathbf{Y},t_n;\mathbf{X},\tau\right)L^b\mathrm{d}\tau \end{aligned} \tag{15}$$

According to the time translation property of the fundamental solution (Wu 2000):

$$p^*(\mathbf{Y},t;\mathbf{X},\tau) = p^*(\mathbf{Y},t+\Delta t;\mathbf{X},\tau+\Delta t) \tag{16}$$

we can further derive the following equations:

$$\begin{aligned} {}^{(b)}P^{(n)(m)}(\mathbf{Y};\mathbf{X}) &= {}^{(b)}P^{(n-1)(m-1)}(\mathbf{Y};\mathbf{X}) = \cdots = {}^{(b)}P^{(n-m+1)(1)}(\mathbf{Y};\mathbf{X}) \\ {}^{(b)}Q^{(n)(m)}(\mathbf{Y};\mathbf{X}) &= {}^{(b)}Q^{(n-1)(m-1)}(\mathbf{Y};\mathbf{X}) = \cdots = {}^{(b)}Q^{(n-m+1)(1)}(\mathbf{Y};\mathbf{X}) \end{aligned} \tag{17}$$

Here, ${}^{(b)}P^{(n-m+1)(1)}$ and ${}^{(b)}Q^{(n-m+1)(1)}$ mean that the calculations for ${}^{(b)}P^{(n)(m)}$ and ${}^{(b)}Q^{(n)(m)}$ only need to be implemented in the first time step ($m=1$). Substituting Eqs. (8) and (9) into Eq. (15) yields:

$$\begin{aligned} {}^{(1)}P^{(n)(1)}(\mathbf{Y};\mathbf{X}) &= \frac{1}{4\pi r}\left(1-n+\frac{r}{c\Delta t}\right) \\ {}^{(2)}P^{(n)(1)}(\mathbf{Y};\mathbf{X}) &= \frac{1}{4\pi r}\left(n-\frac{r}{c\Delta t}\right) \\ {}^{(1)}Q^{(n)(1)}(\mathbf{Y};\mathbf{X}) &= \frac{(n-1)}{4\pi r^2}\frac{\partial r}{\partial \mathbf{n}} \\ {}^{(2)}Q^{(n)(1)}(\mathbf{Y};\mathbf{X}) &= -\frac{n}{4\pi r^2}\frac{\partial r}{\partial \mathbf{n}} \end{aligned} \tag{18}$$

For the discretization in the spatial domain, the eight-node shell element proposed in Appendix 1 is still adopted here. Besides, the mesh of the structural boundary is consistent with that used in the analysis of dynamic response. Consequently, the discrete expression can be further rewritten as follows:

$$\begin{aligned} &\Theta(\mathbf{Y})p\left(\mathbf{Y},t_n\right) + \sum_{m=1}^{n}\sum_{b=1}^{2}\sum_{e=1}^{\bar{e}} \int_{\Gamma_e} {}^{(b)}Q^{(n-m+1)(1)}(\mathbf{Y};\mathbf{X}) \sum_{i=1}^{8} N_i p_{ei}^{b(m)}(\mathbf{X})\mathrm{d}\Gamma_e \\ &= \sum_{m=1}^{n}\sum_{b=1}^{2}\sum_{e=1}^{\bar{e}} \int_{\Gamma_e} {}^{(b)}P^{(n-m+1)(1)}(\mathbf{Y};\mathbf{X}) \sum_{i=1}^{8} N_i q_{ei}^{b(m)}(\mathbf{X})\mathrm{d}\Gamma_e \end{aligned} \tag{19}$$

where the subscripts e and i denote the eth boundary element and the ith element node, respectively; and $\bar{e}$ is the number of elements. We can further transform Eq. (19) into the following algebraic equation:

$$\overline{\boldsymbol{\Theta}}\mathbf{p}^{(n)} + \sum_{m=1}^{n}\sum_{b=1}^{2} {}^{(b)}\mathbf{H}^{(n-m+1)}\mathbf{p}^{(b_g)} = \sum_{m=1}^{n}\sum_{b=1}^{2} {}^{(b)}\mathbf{G}^{(n-m+1)}\mathbf{q}^{(b_g)} \tag{20}$$

where $\mathbf{p}^{(b_g)}$ and $\mathbf{q}^{(b_g)}$ are the vectors containing the sound pressure and sound flux values of all boundary points at the b_gth global time point, respectively; $\mathbf{H}$ and $\mathbf{G}$ are both the coefficient matrices; and $\overline{\boldsymbol{\Theta}}$ represents the matrix containing the values of Θ at all boundary points. Here, the two time interpolation points taken at each time step are the initial and end time points. Thus, $p^{b(m)}$ with $b = 1$ in Eq. (19) corresponds to the sound pressure at the global time point t_{m-1}. In addition, $p^{2(m)}$ corresponds to the sound pressure at the global time point t_m. These rules are also suitable for the sound flux. For this reason, the following new discrete form can be obtained:

$$\sum_{m=1}^{n}\sum_{b=1}^{2}{}^{(b)}\mathbf{H}^{(n-m+1)}\mathbf{p}^{(b_g)}$$
$$=\left({}^{(1)}\mathbf{H}^{(n)}\mathbf{p}^{(0)}+{}^{(2)}\mathbf{H}^{(n)}\mathbf{p}^{(1)}\right)+\cdots+\left({}^{(1)}\mathbf{H}^{(1)}\mathbf{p}^{(n-1)}+{}^{(2)}\mathbf{H}^{(1)}\mathbf{p}^{(n)}\right)$$
$$={}^{(1)}\mathbf{H}^{(n)}\mathbf{p}^{(0)}+\left({}^{(2)}\mathbf{H}^{(n)}+{}^{(1)}\mathbf{H}^{(n-1)}\right)\mathbf{p}^{(1)}+\cdots+{}^{(2)}\mathbf{H}^{(1)}\mathbf{p}^{(n)} \tag{21}$$

Similarly:

$$\sum_{m=1}^{n}\sum_{b=1}^{2}{}^{(b)}\mathbf{G}^{(n-m+1)}\mathbf{q}^{(b_g)}={}^{(1)}\mathbf{G}^{(n)}\mathbf{q}^{(0)} \tag{22}$$
$$+\left({}^{(2)}\mathbf{G}^{(n)}+{}^{(1)}\mathbf{G}^{(n-1)}\right)\mathbf{q}^{(1)}+\cdots+{}^{(2)}\mathbf{G}^{(1)}\mathbf{q}^{(n)}$$

Substituting Eqs. (21) and (22) into Eq. (20) yields:

$$\left({}^{(2)}\mathbf{H}^{(1)}+\overline{\mathbf{\Theta}}\right)\mathbf{p}^{(n)}$$
$$={}^{(1)}\mathbf{G}^{(n)}\mathbf{q}^{(0)}+\left({}^{(2)}\mathbf{G}^{(n)}+{}^{(1)}\mathbf{G}^{(n-1)}\right)\mathbf{q}^{(1)}+\cdots+{}^{(2)}\mathbf{G}^{(1)}\mathbf{q}^{(n)}$$
$$-{}^{(1)}\mathbf{H}^{(n)}\mathbf{p}^{(0)}-\left({}^{(2)}\mathbf{H}^{(n)}+{}^{(1)}\mathbf{H}^{(n-1)}\right)\mathbf{p}^{(1)}-\cdots-\left({}^{(2)}\mathbf{H}^{(2)}+{}^{(1)}\mathbf{H}^{(1)}\right)\mathbf{p}^{(n-1)} \tag{23}$$

Therefore, the transient sound pressure can be iteratively solved by using Eqs. (11) and (23).

4 Description of the time-domain sound radiation design optimization

The purpose of the design optimization in this paper is to seek the optimal ply thicknesses under certain constraints to reduce the time-domain sound radiation. For a given spatial domain Ω_0 that can be either a prescribed reference surface in the sound medium or a vibrating structure surface, the square of sound pressure p^2 over a time period of interest $\left[\mathrm{t}_0,\ \mathrm{t}_1\right]$ as formulated in Eq. (24) is taken as the objective function.

$$f=\int_{\Omega_0}\int_{t_0}^{t_1}p^2(\Omega,t)\,\mathrm{d}t\mathrm{d}\Omega \tag{24}$$

To facilitate the calculation, this time period is uniformly divided into N_t time interpolation points, and the spatial domain is also discretized into N_s spatial nodes. Thus, the discrete form of the above equation can be stated as:

$$f_{dis}=\sum_{i=1}^{N_s}\sum_{j=1}^{N_t}p_{ij}^2\Delta t\Delta\Omega \tag{25}$$

where p_{ij} is the sound pressure of the ith spatial node at the jth time point; Δt is the time interval between two time points; and $\Delta\Omega$ is a discrete space domain.

Note that the vibration response and sound radiation of a laminated structure are closely related to the structural ply thickness. For this reason, designating ply thicknesses as design variables can effectively reduce time-domain noise. In general, light weight is highly desirable in engineering applications, thus structural mass should be strictly limited. Besides, the upper and lower limits of a single ply thickness should also be constrained to satisfy actual requirements. In summary, this design optimization model can be expressed as follows:

$$\begin{aligned}
&\text{Find: }\mathbf{T}=\left(T_1,\ldots,T_g,\ldots,T_{\overline{g}}\right)\\
&\text{Min: }f(\mathbf{T})=\int_{\Omega_0}\int_{t_0}^{t_1}p^2(\Omega,t)\,\mathrm{d}t\mathrm{d}\Omega\\
&\text{or}\\
&f_{dis}(\mathbf{T})=\sum_{i=1}^{N_s}\sum_{j=1}^{N_t}p_{ij}^2\Delta t\Delta\Omega\\
&\text{s.t: }\mathrm{M}\le\overline{\mathrm{M}}\\
&\underline{T}\le T_g\le\overline{T}\ g=1,2,\ldots,\overline{g}
\end{aligned} \tag{26}$$

where $\mathbf{T}$ is the thickness variable vector; T_g is the gth ply thickness variable; $\overline{g}$ is the number of variables; M is the mass of structure, and $\overline{\mathrm{M}}$ is the maximum allowable value of this mass; $\overline{T}$ and $\underline{T}$ are the maximum and minimum thicknesses, respectively, of a single ply.

In this paper, the MMA algorithm based on the sensitivity information is applied to solve for the optimization problem. In the model (26), the sensitivity formula of the discrete objective function with respect to the design variable T_g can be written as:

$$\frac{\partial f_{dis}}{\partial T_g}=\sum_{i=1}^{N_s}\sum_{j=1}^{N_t}2p_{ij}\frac{\partial p_{ij}}{\partial T_g}\Delta t\Delta\Omega \tag{27}$$

It is worth mentioning that the core of Eq. (27) is the term $\partial p_{ij}/\partial T_g$. Indeed, the transient sound pressure is the most common and classic measurement index used in time-domain sound radiation analysis, which is the reason why transient sound pressure is selected as the optimization goal in this paper. For other cost functions such as the sound power, sound intensity, etc., we need to merely express their derivatives as a form including the term $\partial p_{ij}/\partial T_g$, and no further changes in other sensitivity equations are required. The detailed sensitivity derivation of sound pressure will be given in the next section. In addition, the sensitivity of the structural mass with respect to ply thickness variable is equal to the area of this ply multiplied by the mass density.

5 Sensitivity analysis for transient sound radiation

The sensitivity analysis is a necessary condition to obtain optimal designs by using gradient optimization algorithms. In this section, the sensitivity formulae for transient sound pressure with respect to ply thickness are derived by using a direct method. In Eq. (20), the matrix $\overline{\mathbf{\Theta}}$ is merely related to the structural surface shape, and both the matrices $\mathbf{H}$ and $\mathbf{G}$ only depend on the initial state of sound field, which means that their derivative values with respect to the ply thickness are all equal to zero. Hence, the following expression can be obtained by taking the derivatives on both sides of Eq. (20) with respect to the ply thickness variable T_g:

$$\overline{\boldsymbol{\Theta}}\frac{\partial \mathbf{p}^{(n)}}{\partial T_g}+\sum_{m=1}^{n}\sum_{b=1}^{2}{}^{b(m)}\mathbf{H}^{(n-m+1)}\frac{\partial \mathbf{p}^{(b_g)}}{\partial T_g}=\sum_{m=1}^{n}\sum_{b=1}^{2}{}^{b(m)}\mathbf{G}^{(n-m+1)}\frac{\partial \mathbf{q}^{(b_g)}}{\partial T_g} \tag{28}$$

Note that the above equation has the same structural form as Eq. (20), thus the same solution approach can still be employed here. Therefore, taking the derivative of Eq. (23) yields:

$$\begin{aligned}&\left({}^{(2)}\mathbf{H}^{(1)}+\overline{\boldsymbol{\Theta}}\right)\frac{\partial \mathbf{p}^{(n)}}{\partial T_g}\\&={}^{(1)}\mathbf{G}^{(n)}\frac{\partial \mathbf{q}^{(0)}}{\partial T_g}+\left({}^{(2)}\mathbf{G}^{(n)}+{}^{(1)}\mathbf{G}^{(n-1)}\right)\frac{\partial \mathbf{q}^{(1)}}{\partial T_g}+\cdots+{}^{(2)}\mathbf{G}^{(1)}\frac{\partial \mathbf{q}^{(n)}}{\partial T_g}\\&-{}^{(1)}\mathbf{H}^{(n)}\frac{\partial \mathbf{p}^{(0)}}{\partial T_g}-\left({}^{(2)}\mathbf{H}^{(n)}+{}^{(1)}\mathbf{H}^{(n-1)}\right)\frac{\partial \mathbf{p}^{(1)}}{\partial T_g}-\cdots-\left({}^{(2)}\mathbf{H}^{(2)}+{}^{(1)}\mathbf{H}^{(1)}\right)\frac{\partial \mathbf{p}^{(n-1)}}{\partial T_g}\end{aligned} \tag{29}$$

To calculate $\partial \mathbf{q}^{(n)}/\partial T_g$, the derivative of Eq. (11) is carried out; this yields to

$$\frac{\partial \mathbf{q}^{(n)}}{\partial T_g}=-\rho_a\frac{\partial \ddot{\mathbf{u}}_{\mathrm{N}}^{(n)}}{\partial T_g} \tag{30}$$

Accordingly, the problem of solving for the transient sound pressure sensitivity is transformed into the problem of solving for the transient dynamic response sensitivity.

Furthermore, the following equations can be derived by taking the derivatives of both Eqs. (4) and (5):

$$\tilde{\mathbf{K}}\frac{\partial \mathbf{u}^{(n+1)}}{\partial T_g}=\frac{\partial \tilde{\mathbf{F}}^{(n+1)}}{\partial T_g}-\frac{\partial \tilde{\mathbf{K}}}{\partial T_g}\mathbf{u}^{(n+1)} \tag{31}$$

with

$$\begin{aligned}\frac{\partial \tilde{\mathbf{K}}}{\partial T_g}&=\frac{\partial \mathbf{K}}{\partial T_g}+\psi_0\frac{\partial \mathbf{M}}{\partial T_g}+\psi_1\frac{\partial \mathbf{C}}{\partial T_g}\\\frac{\partial \tilde{\mathbf{F}}^{(n+1)}}{\partial T_g}&=\frac{\partial \mathbf{F}^{(n+1)}}{\partial T_g}+\frac{\partial \mathbf{M}}{\partial T_g}\left(\psi_0\mathbf{u}^{(n)}+\psi_2\dot{\mathbf{u}}^{(n)}+\psi_3\ddot{\mathbf{u}}^{(n)}\right)\\&+\frac{\partial \mathbf{C}}{\partial T_g}\left(\psi_1\mathbf{u}^{(n)}+\psi_4\dot{\mathbf{u}}^{(n)}+\psi_5\ddot{\mathbf{u}}^{(n)}\right)\\&+\mathbf{C}\left(\psi_1\frac{\partial \mathbf{u}^{(n)}}{\partial T_g}+\psi_4\frac{\partial \dot{\mathbf{u}}^{(n)}}{\partial T_g}+\psi_5\frac{\partial \ddot{\mathbf{u}}^{(n)}}{\partial T_g}\right)\\&+\mathbf{M}\left(\psi_0\frac{\partial \mathbf{u}^{(n)}}{\partial T_g}+\psi_2\frac{\partial \dot{\mathbf{u}}^{(n)}}{\partial T_g}+\psi_3\frac{\partial \ddot{\mathbf{u}}^{(n)}}{\partial T_g}\right)\end{aligned} \tag{32}$$

In this paper, the external force is independent of ply thickness, thus $\partial \mathbf{F}/\partial T_g$ is equal to zero here. Based on Equation (A6), the derivative of element stiffness matrix is depicted as

$$\frac{\partial \mathbf{K}^e}{\partial T_g}=\sum_{k=1}^{\bar{k}}\frac{\partial \mathbf{K}_k^e}{\partial T_g} \tag{33}$$

where $\mathbf{K}_k^e$ is the stiffness matrix of the kth ply belonging to the eth element. For curved shell elements, $\mathbf{B}_k$, $|\mathbf{J}|_k$, and $|\mathbf{J}^*|_k$ in Equation (A6) are all the functions of ply thickness. Thus, the detailed expression of Eq. (33) is given by

$$\frac{\partial \mathbf{K}_k^e}{\partial T_g}=\int_{-1}^{1}\int_{-1}^{1}\int_{-1}^{1}\begin{pmatrix}\frac{\partial \mathbf{B}_k^{\mathrm{T}}}{\partial T_g}\overline{\mathbf{D}}_k\mathbf{B}_k|\mathbf{J}|_k|\mathbf{J}^*|_k+\mathbf{B}_k^{\mathrm{T}}\overline{\mathbf{D}}_k\frac{\partial \mathbf{B}_k}{\partial T_g}|\mathbf{J}|_k|\mathbf{J}^*|_k\\+\mathbf{B}_k^{\mathrm{T}}\overline{\mathbf{D}}_k\mathbf{B}_k\frac{\partial |\mathbf{J}|_k}{\partial T_g}|\mathbf{J}^*|_k+\mathbf{B}_k^{\mathrm{T}}\overline{\mathbf{D}}_k\mathbf{B}_k|\mathbf{J}|_k\frac{\partial |\mathbf{J}^*|_k}{\partial T_g}\end{pmatrix}\mathrm{d}\xi\mathrm{d}\eta\mathrm{d}\zeta^* \tag{34}$$

Here, $\partial \mathbf{B}_k/\partial T_g$ and $\partial|\mathbf{J}^*|_k/\partial T_g$ can be obtained by taking derivatives of Equations (A12) and (A10), respectively. In addition, $\partial|\mathbf{J}|_k/\partial T_g$ can be calculated by using Equation (A11) and the derivative rules of determinant. By differentiating Eq. (3), the derivatives of transient dynamic responses are written as:

$$\begin{aligned}\frac{\partial \dot{\mathbf{u}}^{(n+1)}}{\partial T_g}&=\frac{\partial \dot{\mathbf{u}}^{(n)}}{\partial T_g}+\left[(1-\delta)\frac{\partial \ddot{\mathbf{u}}^{(n)}}{\partial T_g}+\delta\frac{\partial \ddot{\mathbf{u}}^{(n+1)}}{\partial T_g}\right]\Delta t\\\frac{\partial \mathbf{u}^{(n+1)}}{\partial T_g}&=\frac{\partial \mathbf{u}^{(n)}}{\partial T_g}+\frac{\partial \dot{\mathbf{u}}^{(n)}}{\partial T_g}\Delta t+\left[(0.5-\gamma)\frac{\partial \ddot{\mathbf{u}}^{(n)}}{\partial T_g}+\gamma\frac{\partial \ddot{\mathbf{u}}^{(n+1)}}{\partial T_g}\right](\Delta t)^2\end{aligned} \tag{35}$$

Therefore, the acceleration sensitivity $\partial \ddot{\mathbf{u}}/\partial T_g$ at each time point can be iteratively solved by using the above equations. In addition, $\partial \ddot{\mathbf{u}}_N/\partial T_g$ which is needed in Eq. (30) is obtained by multiplying $\partial \ddot{\mathbf{u}}/\partial T_g$ by normal cosine vector. Finally, we substitute the results $\partial \mathbf{q}/\partial T_g$ obtained from Eq. (30) into Eq. (29) to calculate $\partial \mathbf{p}/\partial T_g$. Accordingly, the whole process of the optimization strategy can be represented by the flowchart as shown in Fig. 2. Moreover, the optimization iteration loop is stopped when variables show no further obvious change.

In fact, the FEM and time-domain BEM codes can be used as a black box, which means that we only need to access them without modification throughout the whole optimization process. In this way, the sensitivity of the transient dynamic response is calculated by first assembling the right term of Eq. (31) outside the black box of the FEM and then inputting it into the black box of the FEM. Similarly, the sensitivity calculation of transient sound pressure is more convenient. It requires no additional external operations and only recalls the black box of the time-domain BEM. Thus, the evaluation of sensitivity can be regarded as the post processing implemented on the response calculation.

Note that this paper deals with a sizing optimization problem, which indicates that the number of design variables in this study is basically of the same order of magnitude as the

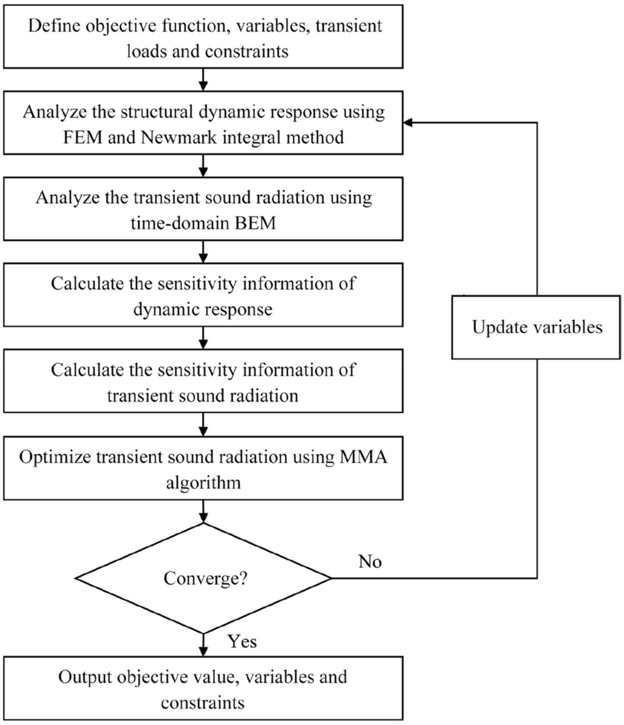

Fig. 2 Flowchart of the design optimization

number of performance measures. Hence, even if the direct method is employed, high computational efficiency can be guaranteed here. Of course, from the perspective of topology optimization with hundreds or even thousands of design variables, using the adjoint variable method is undoubtedly a better choice.

6 Numerical examples

6.1 Verification of the transient sensitivity formulae

In this section, the accuracy of the transient sensitivity formulae is demonstrated by a laminated cylindrical shell structure subjected to a transient load.

As shown in Fig. 3a, we consider a laminated cylindrical shell structure with a height of 0.6 m, a radius of 0.3 m. It has five plies, each with a thickness of 0.002 m, and the ply angles are $[60°, 90°, 0°, 90°, 60°]$. The plies of the structure are orthotropic, and the material properties of this structure and air are shown in Table 1. In addition, the boundary of the bottom surface is completely fixed, and the center node of the top surface is applied with a transient load as shown in Fig. 3b. Note that 101 time points are uniformly distributed in the time domain, and the time interval between two time points is 5×10^{-4} s. Here, the proportional damping $\mathbf{C} = \phi_1\mathbf{M} + \phi_2\mathbf{K}$ with $\phi_1 = 0.2$ and $\phi_2 = 0.003$ is adopted.

In this example, the 1st/5th, 2nd/4th, and 3rd ply thicknesses of this laminated structure are all used as the design variables, and the square of sound pressure of all boundary nodes over the whole loading time period is designated as the objective function. By using the sensitivity formulae derived in this paper, the sensitivity values of the objective function with respect to these three design variables are – 40.79929, – 46.17585, and – 24.13194, respectively. It is worth mentioning that the 3rd ply thickness variable is

Table 1 Properties of structural material and air

Elastic modulus (GPa)	$E_1 = 95.8$, $E_2 = E_3 = 6.7$
Shear modulus (GPa)	$G_{12} = G_{23} = G_{13} = 7.1$
Poisson's ratio	$v_{12} = v_{13} = v_{23} = 0.3$
Structural density (kg/m^3)	$\rho_s = 1800$
Air density (kg/m^3)	$\rho_a = 1.29$
Speed of sound (m/s)	$v_s = 343$

Fig. 3 Sensitivity verification model: **a** laminated cylindrical shell structure, **b** transient force

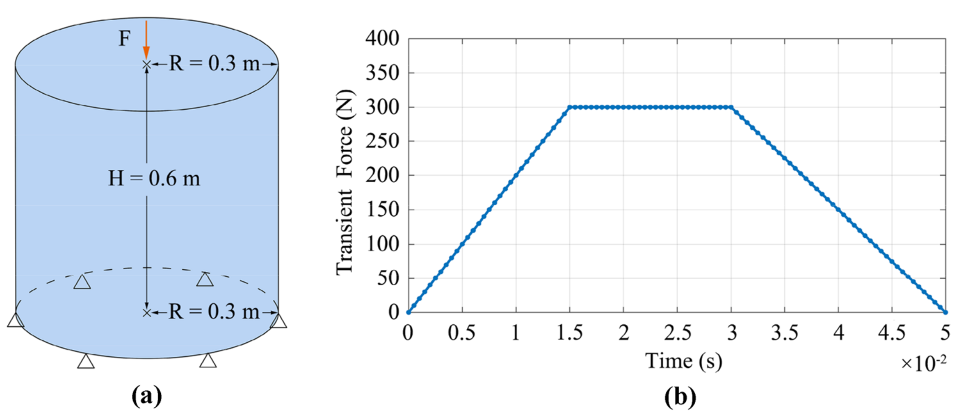

a single ply variable, and thus its sensitivity value is about half of that of the remaining variables.

To verify the accuracy of the sensitivity formulae derived in this paper, the FDM and semi-analytical method are also employed for comparison. The finite difference approximation in FDM can be formulated as (Li and Zheng 2017; Wang et al. 2018):

$$\frac{\partial f}{\partial T_g} = \frac{f\left(T_g+\Delta T_g\right) - f\left(T_g\right)}{\Delta T_g} \tag{36}$$

where ΔT_g is the perturbation step size of the gth design variable. For this study, the essence of the semi-analytical method is to convert the analytical expression (33) into a difference quotient (Lee and Park 1997; Fernandez and Tortorelli 2018):

$$\frac{\partial \mathbf{K}^e}{\partial T_g} = \frac{\mathbf{K}^e\left(T_g+\Delta T_g\right) - \mathbf{K}^e\left(T_g\right)}{\Delta T_g} \tag{37}$$

Note that two sources of error (truncation and condition errors) should be considered here. The former is usually produced by a larger perturbation step size. Contrarily, the latter is generally caused by a very small step size. Taking the FDM as analysis instance, the effects of perturbation step size on sensitivity error are shown in Fig. 4. The relative error is determined by taking the difference between the two sensitivity results and dividing by the result calculated by the method proposed in this paper.

The truncation and condition errors caused by different perturbation step sizes can be clearly seen from Fig. 4. Hence, an adequate perturbation step size is worthy of consideration. By referring to the literature (Iott et al. 1985), we can determine the near-optimum perturbation step sizes of 2.82×10^{-10} m, 2.48×10^{-10} m, and 4.61×10^{-10} m for these three design variables. After calculation, the sensitivity values and relative errors are listed in Table 2 and the transient sensitivities at each time point are shown in Fig. 5.

It can be apparently seen that the sensitivity results calculated by the method proposed in this paper are basically consistent with those calculated by the FDM and semi-analytical method with a near-optimum perturbation step size. Note that the sensitivity formulae in this paper are derived by directly differentiating the response equations, see sensitivity Eqs. (28) and (31). For this reason, the same numerical method can be conveniently used to solve for the sensitivity values, the perturbed and unperturbed responses. Thus, the difference between the sensitivity results calculated by using the method proposed in this paper and FDM or semi-analytical method is merely caused by the choice of perturbation step size. Nonetheless, even if a near-optimum perturbation step size is used, we still cannot completely eliminate the truncation and condition errors, which can be seen from those extremely small relative errors in Table 2. In addition, the direct method employed in this paper is a kind of analytical method. As described in

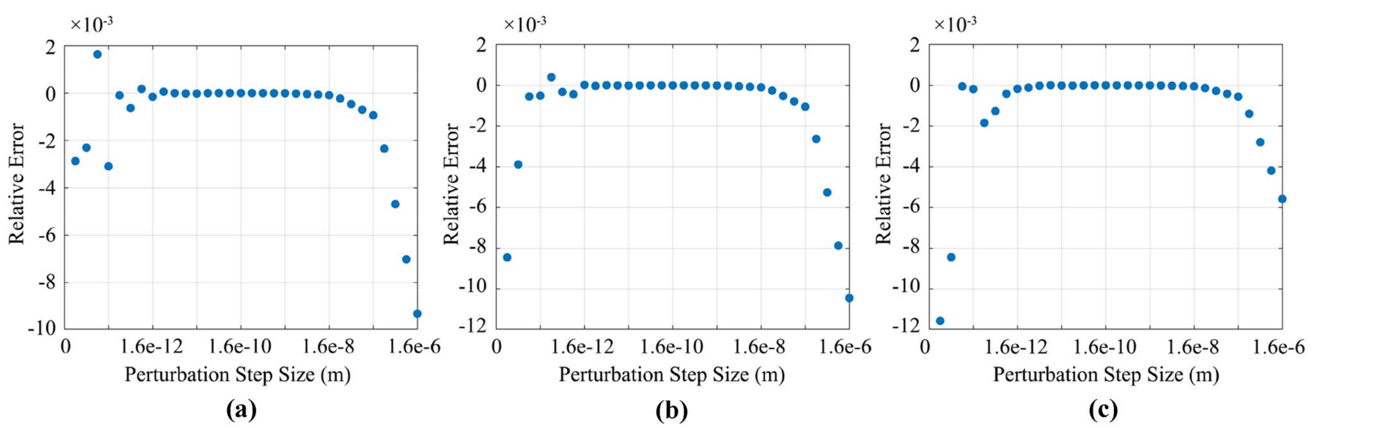

Fig. 4 Effects of perturbation step size in FDM on sensitivity error: **a** the 1st/5th ply thickness variable, **b** the 2nd/4th ply thickness variable, **c** the 3rd ply thickness variable

Table 2 Sensitivity comparison

Design variables	This paper	FDM	Relative errors	Semi-analytical method	Relative errors
The 1st/5th ply thicknesses	−40.79929	−40.79899	7.35×10^{-6}	−40.79928	2.45×10^{-7}
The 2nd/4th ply thicknesses	−46.17585	−46.17574	2.38×10^{-6}	−46.17585	8.01×10^{-8}
The 3rd ply thickness	−24.13194	−24.13181	5.39×10^{-6}	−24.13193	4.14×10^{-7}

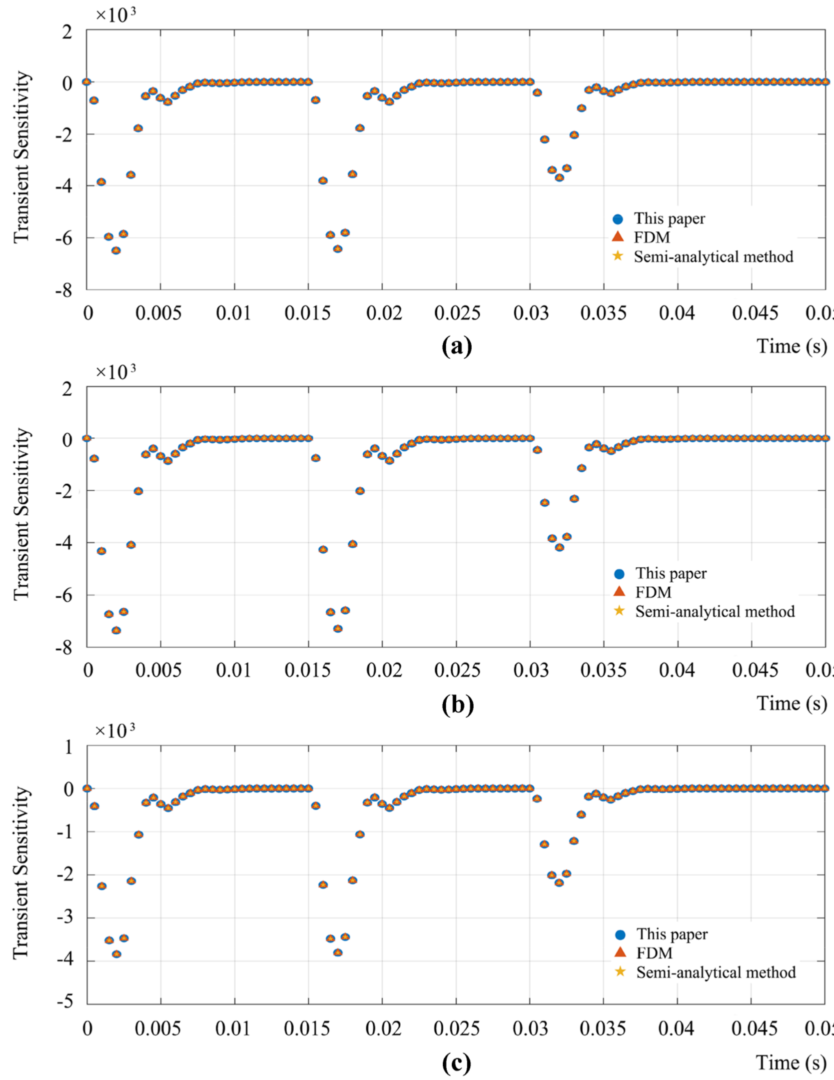

Fig. 5 Transient sensitivities: **a** the 1st/5th ply thickness variable, **b** the 2nd/4th ply thickness variable, **c** the 3rd ply thickness variable

the literature (Martins and Hwang 2013), "the numerical precision of analytical methods is the same as that of the original algorithm". Compared with frequency-domain analysis, the responses at each time point need to be iteratively calculated in time-domain analysis, which could produce numerical instability and accumulated error. To avoid these potential problems of original algorithm, we adopt the Newmark integral method which is an implicit algorithm to solve for transient dynamic responses and determine the adequate time step size used in time-domain sound radiation analysis by referring to the literature (Wu 2000).

6.2 Time-domain sound radiation design optimization of laminated curved shell structures

6.2.1 Design optimization of a truncated cone structure

6.2.1.1 Discussion for different transient loads As shown in Fig. 6, a laminated truncated cone shell structure with a height of 0.6 m in the Cartesian coordinate system is considered. The top surface diameter and bottom surface diameter of the structure are 0.4 m and 0.8 m, respectively, and the

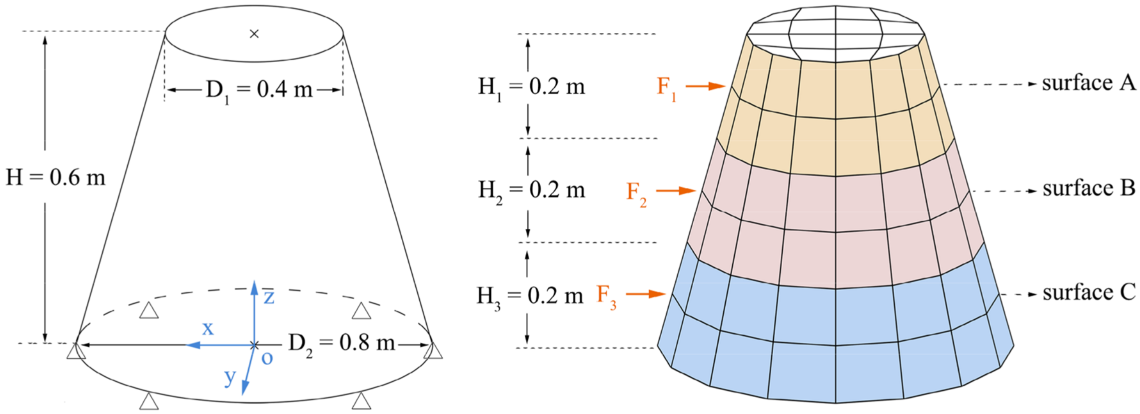

Fig. 6 Laminated truncated cone shell structure

center node of the bottom surface is the coordinate origin. The structure is divided into 128 eight-node shell elements with 386 nodes. The inclined surface is divided into three design domains: the surface A with an area of 0.31 m^2, the surface B with an area of 0.40 m^2, and the surface C with an area of 0.49 m^2. The remaining top and bottom surfaces are non-design domains. Furthermore, this structure has five plies, each with a thickness of 0.002 m, and the ply angles are $[60°, 90°, 0°, 90°, 60°]$. The structural plies are orthotropic, and the corresponding material properties and air properties are shown in Table 1. In addition, the boundary of the bottom surface is completely fixed. To analyze the optimal results of ply thickness for different transient forces and loading positions, the following four cases are considered:

Case 1: only the transient force F_1 is applied.

Case 2: only the transient force F_2 is applied.

Case 3: only the transient force F_3 is applied.

Case 4: the transient forces F_1, F_2, and F_3 are applied simultaneously.

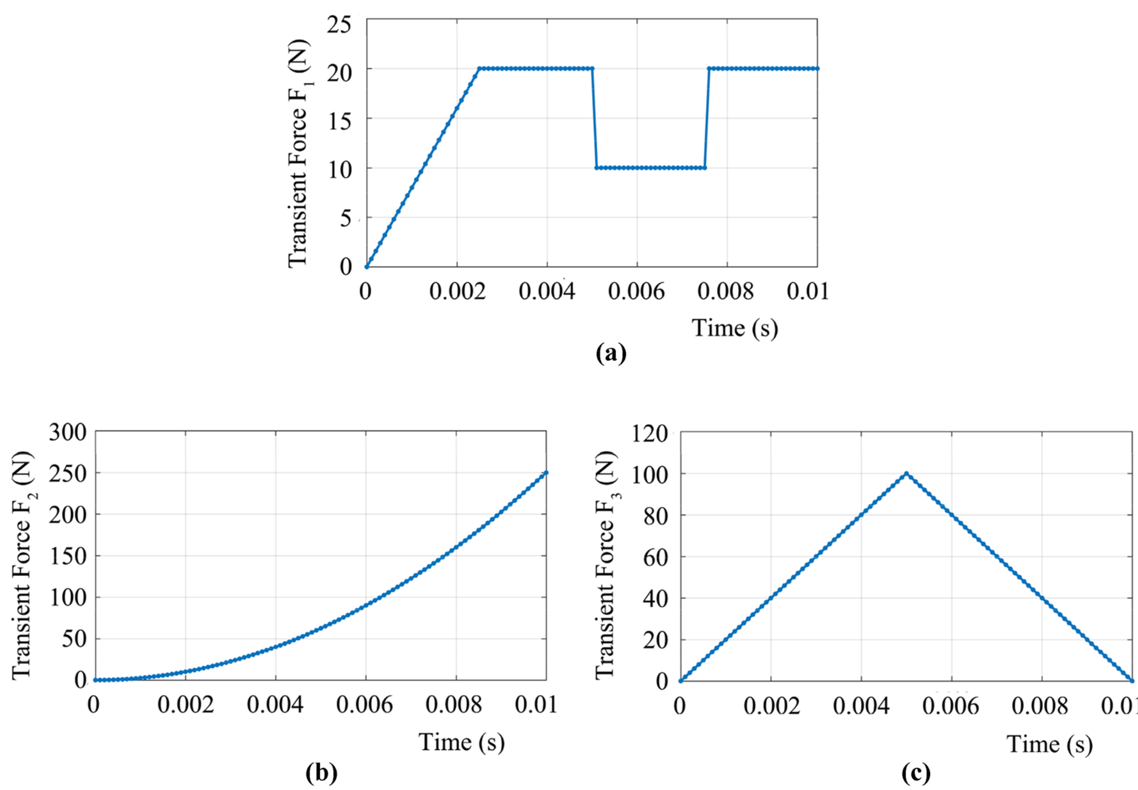

Fig. 7 Different transient forces: **a** transient force F_1, **b** transient force F_2, **c** transient force F_3

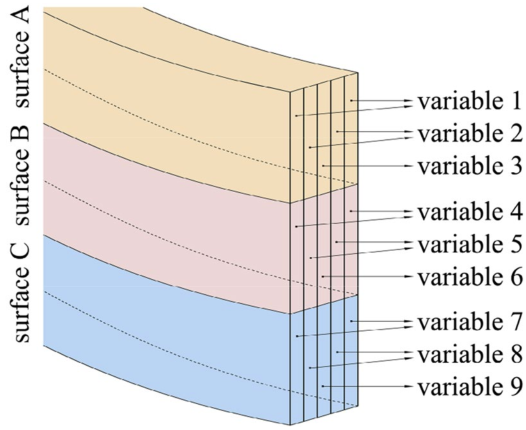

Fig. 8 Nine design variables

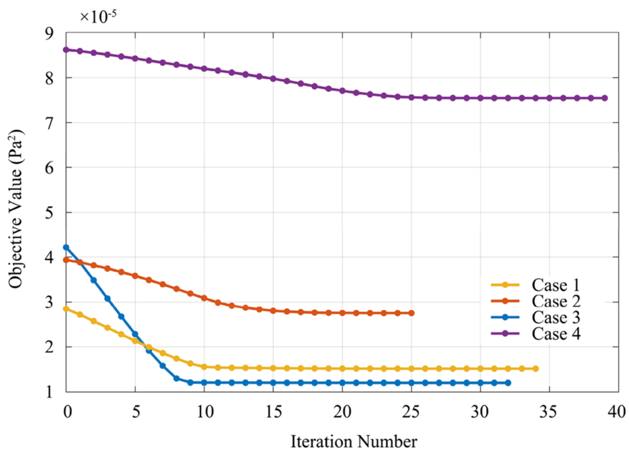

Fig. 9 Iteration histories for four cases

Figure 7 shows these three transient forces. In addition, there are 101 time interpolation points uniformly distributed in the time domain, and the time interval between two time points is 1×10^{-4} s. Here, the same damping form as in Sect. 6.1 is adopted.

In this example, the square of sound pressure on surfaces A, B, and C over the whole loading time period is taken as the objective function. Due to the symmetry of the structural plies, the thicknesses of the two plies symmetrical to each other are taken as one design variable. Therefore, for each structural surface among design domains, the 1st/5th ply thicknesses, the 2nd/4th ply thicknesses, and the 3rd ply thickness are all designated as the design variables. All nine design variables are shown in Fig. 8. In addition, the initial structural mass of surfaces A, B, and C is specified as the upper limit of the mass constraint, and the lower and upper limits for each design variable are set to 0.001 m and 0.003 m, respectively. In this example, the optimization iteration is stopped when the maximum absolute value of the changes of design variables between two adjacent iteration steps is less than 0.000001 m.

Figure 9 shows the iteration histories of the objective values for all cases. It can be apparently seen that the objective values are all gradually reduced with the increase of optimization iteration steps and converge finally. Table 3 lists the initial and optimal objective values, design variables and constraint values for all cases. Within the limits of constraints, the objective values for Cases 1 to 4 are decreased by 46.67%, 30.20%, 71.56%, and 12.43%, respectively. Moreover, the structural masses for these four cases all reach the upper limits. Hence, the time-domain noise is still successfully reduced after optimization, although the structural mass is not changed. However, the distributions of variables are different between these four cases. In Case 1, the transient force F_1 is applied on surface A, and the ply thicknesses belonging to this surface all increase to the upper limit. Similarly, in Case 3, all plies of surface C are thickened to the maximum thickness. Besides, the 1st/5th

Table 3 Summary of parameters for the initial and optimal designs

Design parameters	Initial values				Lower limit	Upper limit	Optimal values			
	Case 1	Case 2	Case 3	Case 4			Case 1	Case 2	Case 3	Case 4
Objective value ($\times 10^{-5}$ Pa^2)	2.85	3.94	4.22	8.61	–	–	1.52	2.75	1.20	7.54
Variable 1 (mm)	2.00	2.00	2.00	2.00	1.00	3.00	3.00	1.04	2.06	2.48
Variable 2 (mm)	2.00	2.00	2.00	2.00	1.00	3.00	3.00	1.20	1.63	1.33
Variable 3 (mm)	2.00	2.00	2.00	2.00	1.00	3.00	3.00	1.00	1.01	3.00
Variable 4 (mm)	2.00	2.00	2.00	2.00	1.00	3.00	2.39	3.00	1.00	1.85
Variable 5 (mm)	2.00	2.00	2.00	2.00	1.00	3.00	1.42	2.31	1.07	1.00
Variable 6 (mm)	2.00	2.00	2.00	2.00	1.00	3.00	1.22	3.00	1.00	3.00
Variable 7 (mm)	2.00	2.00	2.00	2.00	1.00	3.00	2.19	3.00	3.00	2.83
Variable 8 (mm)	2.00	2.00	2.00	2.00	1.00	3.00	1.19	1.46	3.00	1.00
Variable 9 (mm)	2.00	2.00	2.00	2.00	1.00	3.00	1.00	1.00	3.00	3.00
Mass (kg)	21.46	21.46	21.46	21.46	10.73	21.46	21.46	21.46	21.46	21.46

and 3rd ply thicknesses reach the maximum values in Case 2, and the 2nd/4th ply thicknesses are also thickened. Therefore, increasing the ply thicknesses of the nodes near the loading positions can effectively reduce sound radiation. In Case 4, these three transient forces are applied simultaneously, thus each design surface has a ply with maximum thickness finally. The optimization results show that the ply thickness distributions are adjusted reasonably within the allowable constraints. In the practical engineering, designers and engineers should pay more attention to adding materials in the areas near the loading positions.

Figure 10 shows the comparisons between the initial and optimal objective curves in the time domain for all cases. The time-domain integrals of these curves are the objective values as shown in Table 3. As shown in Fig. 10a, the longitudinal coordinate values suddenly increase at the time points about 0.005 s and 0.0075 s. The reason is that the transient force F_1 changes significantly at these corresponding time points. Similarly, the longitudinal coordinate values also suddenly increase at the time point about 0.005 s in Case 3. Because the values of the transient force F_2 are the power function of time, the two curves in Case 2 are smooth and do not change suddenly. As shown in Fig. 10d, the longitudinal coordinate values at the time points about 0.005 s and 0.0075 s suddenly increase due to the simultaneous loading of these three transient forces. Moreover, we can see that the optimal curve has a similar shape to the initial curve in each case, but the values of the former are significantly smaller than those of the latter. In addition, in Cases 1 to 4, compared with the initial maximum peak values, the optimal maximum peak values are reduced by 47.42%, 30.44%, 72.56% and 3.94%, respectively. The reduction of peak values means that the noise is more uniform and stable in the time domain. Therefore, the results mean that the

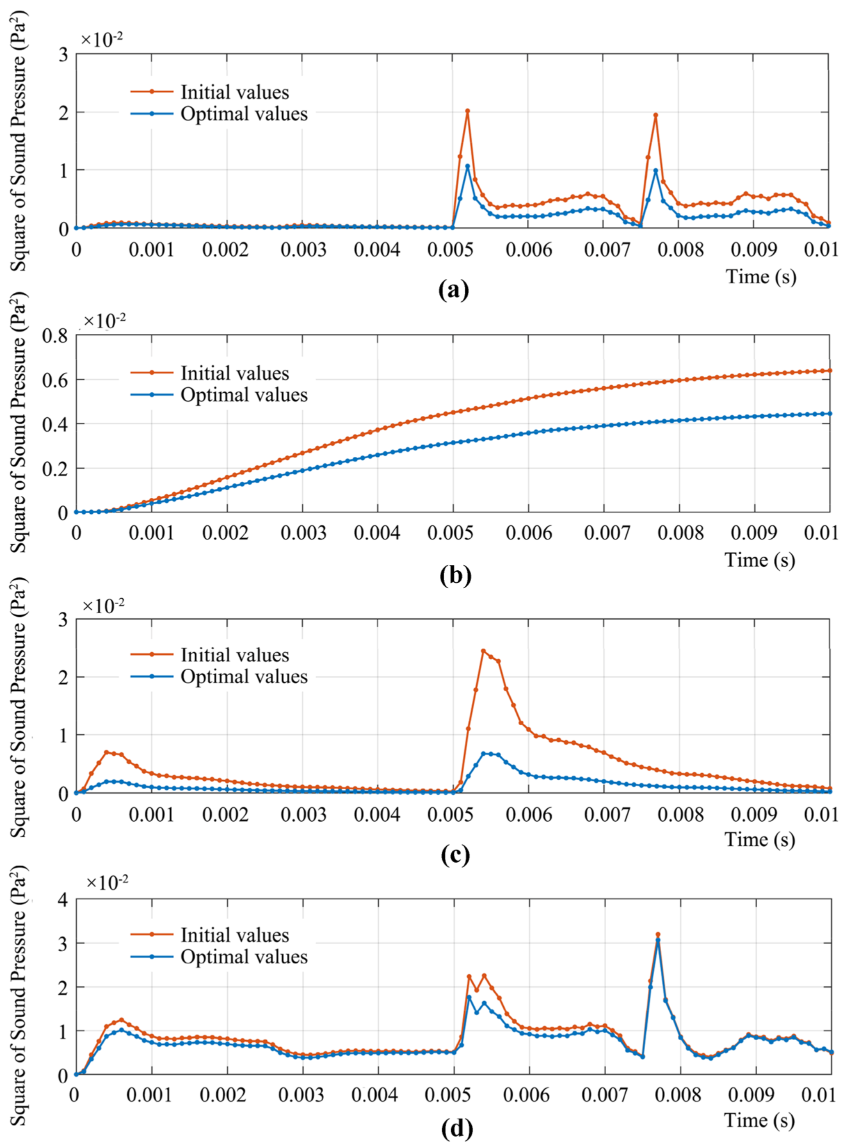

Fig. 10 Comparisons between the initial and optimal objective curves in the time domain: **a** Case 1, **b** Case 2, **c** Case 3, **d** Case 4

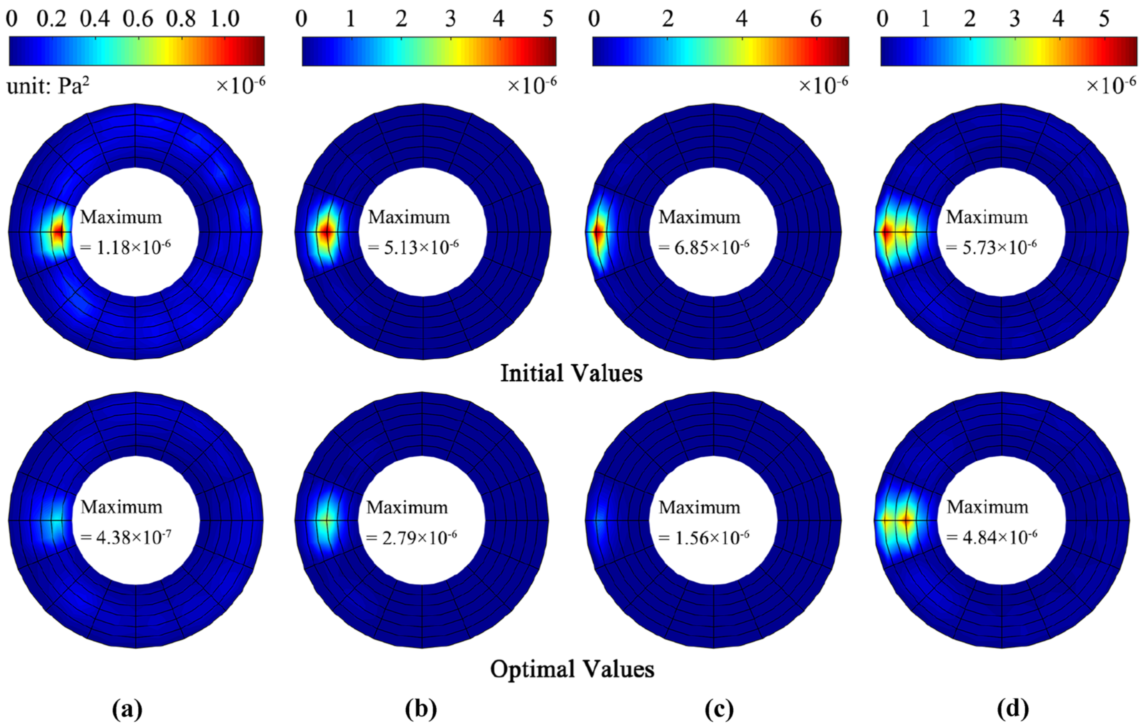

Fig. 11 Nephograms of the initial and optimal sound radiation in all cases (top view): **a** Case 1, **b** Case 2, **c** Case 3, **d** Case 4

time-domain sound radiation is effectively reduced by optimizing the structural ply thicknesses.

Figure 11 shows the initial and optimal nephograms in all cases. For the diagrams of each case, the sum of all nodal values are the objective values as shown in Table 3. After optimization, the average nodal values for Cases 1 to 4 are decreased by 46.67%, 30.20%, 71.56%, and 12.43%, respectively. In addition, the reductions of maximum nodal values are even greater, and they are 62.88%, 45.61%, 77.23%, and 15.53% for Cases 1 to 4, respectively. These results reveal that the distribution of the optimal sound radiation in the spatial domain is more uniform than that of the initial sound radiation. Moreover, we can also see that the larger sound pressure values appear in the areas near the loading nodes, so the optimization of the areas near the loading positions plays an important role in reducing sound radiation.

6.2.1.2 Discussion for different initial values of design variables In this subsection, we take the predefined Case 2 as the instance to analyze the influence of the initial values of design variables on optimal results. First of all, the six groups of different initial values of design variables are listed in Table 4.

Note that the prescribed values of the 2nd group are opposed to the optimal values of the 1st group shown in Table 3, and the values of the 5th and the 6th groups are also opposite in the design domain. By the way, the selection of the initial values does not consider whether the constraint is satisfied. In other words, some values are not located in the feasible design domain. To sum up, the selected starting points are not concentrated in the same domain.

Table 4 Initial values for the six groups

Groups	Initial values of design variables (mm)
1st	[2.000, 2.000, 2.000, 2.000, 2.000, 2.000, 2.000, 2.000, 2.000]
2nd	[3.000, 3.000, 3.000, 1.000, 2.000, 1.000, 1.000, 3.000, 3.000]
3rd	[1.000, 2.000, 3.000, 1.000, 2.000, 3.000, 1.000, 2.000, 3.000]
4th	[3.000, 2.000, 1.000, 3.000, 2.000, 1.000, 3.000, 2.000, 1.000]
5th	[1.000, 1.000, 1.000, 1.000, 1.000, 1.000, 1.000, 1.000, 1.000]
6th	[3.000, 3.000, 3.000, 3.000, 3.000, 3.000, 3.000, 3.000, 3.000]

After calculation, the iteration histories of objective functions for these groups are plotted in Fig. 12. Since the initial objective value of the 5th group is relatively large, the curves of the first three iteration steps of this group are not given here, which does not affect the analysis. Furthermore, the optimal results for these six groups are also shown in Table 5.

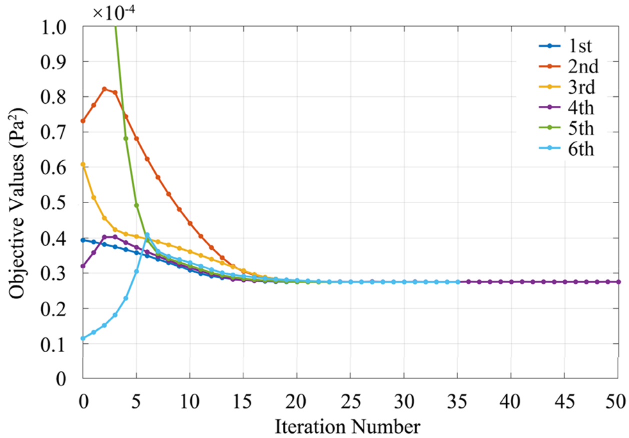

Fig. 12 Iteration histories of objective functions

As seen from Fig. 12, no matter whether the starting point satisfies the constraint, all curves approximately converge to the same value. Besides, it can be seen from Table 5 that the final objective and design variable values of all groups are basically the same. Even for the 4th group, its results are highly close to those of other groups. The results indicate that the selection of the initial values of design variables in this example has little effect on the optimal results.

6.2.1.3 Comparison with the results of SA We know that the result cannot be guaranteed to come from a global minimum under the premise of using the classical MMA based on gradient information, especially for the complex non-convex optimization problem investigated in this paper. Next, we try to use SA to minimize the objective function for comparison. SA is an iterative adaptive heuristic probabilistic search algorithm that can obtain the globally optimal solution with a large probability. The predefined Case 2 is still used here for analysis. Moreover, the detailed parameters in SA can be found in (Zheng et al. 2021). After optimization, the optimal results for the gradient-based method used in this paper and SA are shown in Table 6.

It can be seen that the optimal design variables obtained by using the two schemes are somewhat different, but their optimal values are extremely close. The reason is that the sensitivities of the objective function with respect to the 1st, 2nd, 3rd, 8th, and 9th design variables are very small compared with other design variables. Thus, we can conclude that the result in this example comes from the near-global optimum. However, from the perspective of practical engineering, the primary requirement is reducing noise as much as possible. Although the results in this paper cannot be guaranteed to come from standard globally optimal solutions, the difference between them is still very small, which is sufficient for practical engineering. Moreover, Table 6 shows that the gradient-based method proposed in this paper greatly reduces the computational cost compared with SA, which is also very desirable in practical projects. Thus, the optimization strategy proposed in this paper is effective and reliable.

Table 6 Optimal designs of the two schemes

	Optimal design variables	Optimal values	Time
This paper	[1.035, 1.198, 1.000, 3.000, 2.308, 3.000, 3.000, 1.463, 1.000]	2.74943×10^{-5} Pa^2	2.46 h
SA	[1.149, 1.230, 1.012, 2.997, 2.305, 2.998, 2.998, 1.363, 1.041]	2.74888×10^{-5} Pa^2	20.03 h

6.2.2 Optimization design of a car model

Figure 13 shows a simplified car model and the coordinates of some selected nodes in the Cartesian coordinate system. The car model is divided into 152 eight-node curved shell elements with 458 nodes. The top surface of the car model with an area of 3.63 m^2 is labeled surface A, and the two side surfaces with a total area of 6.51 m^2 are labeled surface B, and the front and back surfaces with a total area of 5.60 m^2 are labeled surface C. The remaining surfaces of the car model are the non-design domains. The car model has five plies, each with a thickness of 0.0025 m, and the ply angles are $[30°, 0°, 90°, 0°, 30°]$. The structural plies are orthotropic, and the structural material and air properties are shown in

Table 5 Optimal results for the six groups

Groups	Optimal design variables (mm)	Optimal objective values (Pa^2)
1st	[1.035, 1.198, 1.000, 3.000, 2.308, 3.000, 3.000, 1.463, 1.000]	2.749426×10^{-5}
2nd	[1.036, 1.198, 1.000, 3.000, 2.309, 3.000, 3.000, 1.462, 1.000]	2.749426×10^{-5}
3rd	[1.035, 1.198, 1.000, 3.000, 2.309, 3.000, 3.000, 1.463, 1.000]	2.749425×10^{-5}
4th	[1.090, 1.183, 1.003, 2.997, 2.308, 2.997, 2.962, 1.473, 1.011]	2.752132×10^{-5}
5th	[1.036, 1.198, 1.000, 3.000, 2.308, 3.000, 3.000, 1.463, 1.000]	2.749426×10^{-5}
6th	[1.036, 1.198, 1.000, 3.000, 2.308, 3.000, 3.000, 1.463, 1.000]	2.749426×10^{-5}

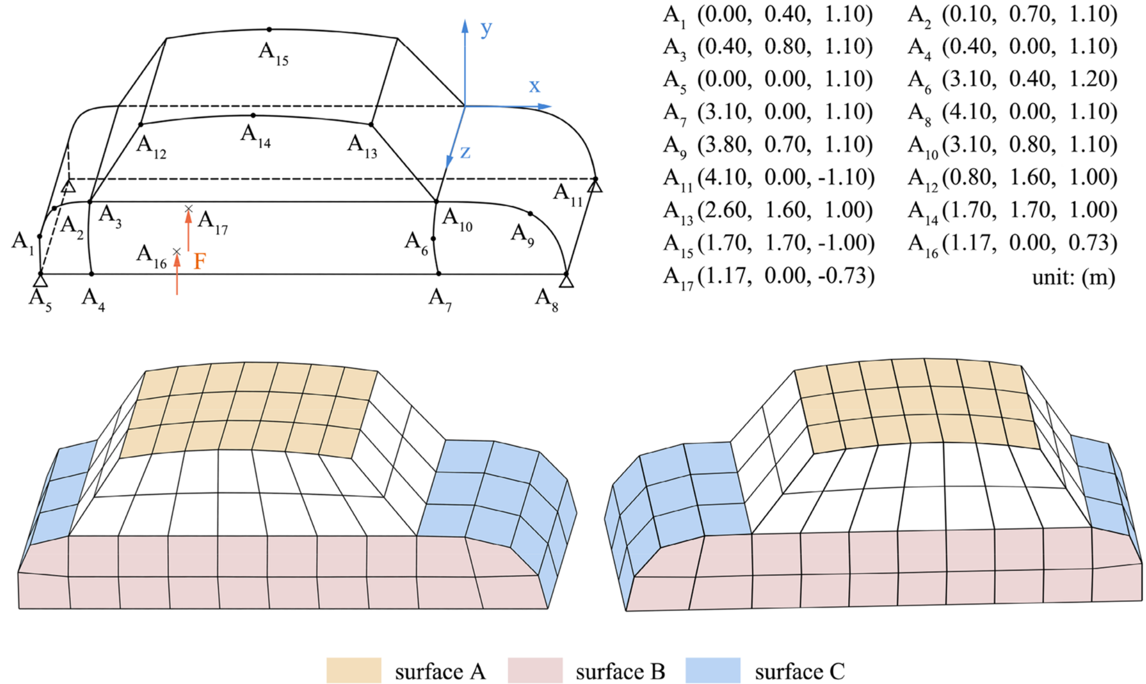

Fig. 13 Laminated car shell model

Table 7 Properties of structural material and air

Elastic modulus (GPa)	$E_1 = 100,\ E_2 = E_3 = 9$
Shear modulus (GPa)	$G_{12} = G_{23} = G_{13} = 4.4$
Poisson's ratio	$\nu_{12} = \nu_{13} = \nu_{23} = 0.27$
Structural density (kg/m^3)	$\rho_s = 1600$
Air density (kg/m^3)	$\rho_a = 1.29$
Speed of sound (m/s)	$v_s = 343$

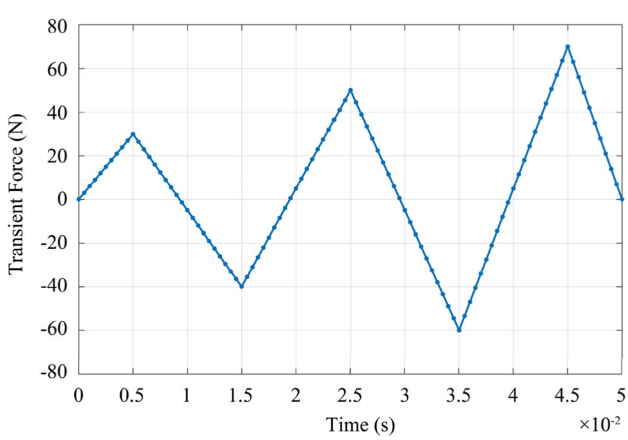

Fig. 14 Transient force

Table 7. In addition, the four corner nodes of the car model are completely fixed, and two identical transient forces as shown in Fig. 14 are simultaneously applied to the nodes A_{16} and A_{17} on the bottom surface. Moreover, there are 101 time interpolation points uniformly distributed in the time domain, and the time interval between two time points is 5×10^{-4} s. Here, the same damping form as in Sect. 6.1 is adopted.

To analyze the noise radiated by the vibrating car model to the surrounding environment in the practical engineering, a reference hemispherical surface with a radius of 5 m as shown in Fig. 15a is considered. The center of this hemisphere surface coincides with the center of the bottom surface of the car model. Here, the hemisphere surface is divided by 48 eight-node elements with 161 nodes as shown in Fig. 15b. In this example, the square of sound pressure of all 161 nodes on the hemispherical surface over the whole loading time period is taken as the objective function. For each surface among design domains, the 1st/5th ply thicknesses, the 2nd/4th ply thicknesses, and the 3rd ply thickness are all specified as the design variables. Moreover, the initial structural mass of surfaces A, B and C is designated as the upper limit of the mass constraint, and the lower and upper limits for a single ply thickness are set to 0.001 m and 0.004 m, respectively. For this example, the optimization iteration is still stopped when the maximum absolute value of the changes of design variables between two adjacent iteration steps is less than 0.000001 m.

Table 8 lists the initial and optimal objective values, design variables and constraint values. After optimization, the objective value is reduced by 28%, and the structural

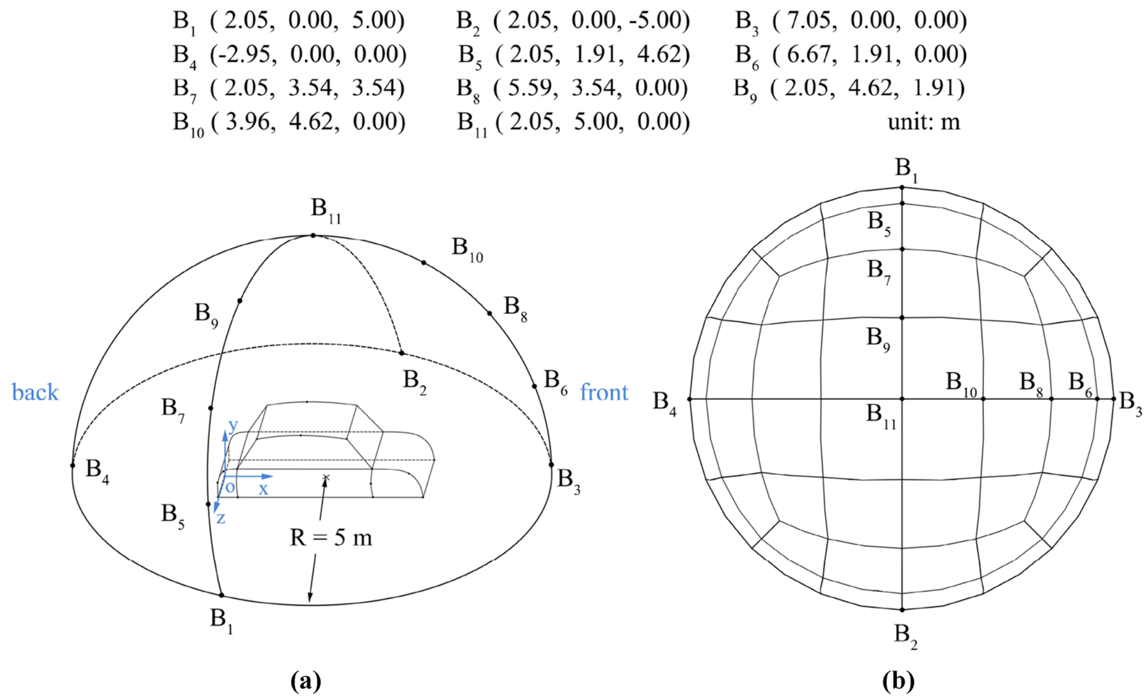

Fig. 15 Reference hemispherical surface: **a** perspective view, **b** mesh division (bottom view)

Table 8 Summary of parameters for the initial and optimal designs

Design parameters	Initial values	Lower limit	Upper limit	Optimal values
Objective value (Pa^2)	3.75×10^{-2}	–	–	2.70×10^{-2}
1st/5th ply thicknesses of surface A (mm)	2.50	1.00	4.00	1.59
2nd/4th ply thicknesses of surface A (mm)	2.50	1.00	4.00	1.72
3rd ply thickness of surface A (mm)	2.50	1.00	4.00	4.00
1st/5th ply thicknesses of surface B (mm)	2.50	1.00	4.00	4.00
2nd/4th ply thicknesses of surface B (mm)	2.50	1.00	4.00	4.00
3rd ply thickness of surface B (mm)	2.50	1.00	4.00	4.00
1st/5th ply thicknesses of surface C (mm)	2.50	1.00	4.00	1.00
2nd/4th ply thicknesses of surface C (mm)	2.50	1.00	4.00	1.00
3rd ply thickness of surface C (mm)	2.50	1.00	4.00	1.00
Mass (kg)	314.72	125.89	314.72	314.72

mass reaches the upper limit. These results show that the time-domain noise is successfully reduced after optimization, although the structural mass is not changed. Different from the selection of design domains in example 6.2.1, the surface applied by the transient forces directly in this example is not used as the design domain. As can be seen from Table 8, the ply thicknesses of surface B all increase to their upper limits. Besides, increasing the ply thicknesses of surface A is also conducive to reducing the sound radiation.

Figure 16a shows the iteration curves about the objective value and structural mass. We can see that the objective value is gradually reduced with the increase of optimization iteration step and converges finally. In addition, the structural mass is always within the constraint and reaches the upper limit value finally. Figure 16b shows the nephograms at different iteration steps. The nodes B_1, B_2, and B_3 mark the direction of the reference hemispherical surface, and they can be found in Fig. 15. It can be seen that the noise from the front direction of the car model is larger than that from both the sides and back directions. Moreover, the position with the minimum value remains unchanged and is located at the node No.16, while the position with the maximum value changes slightly. In the initial iteration step, the node with the maximum sound radiation is No. 21, whereas it moves

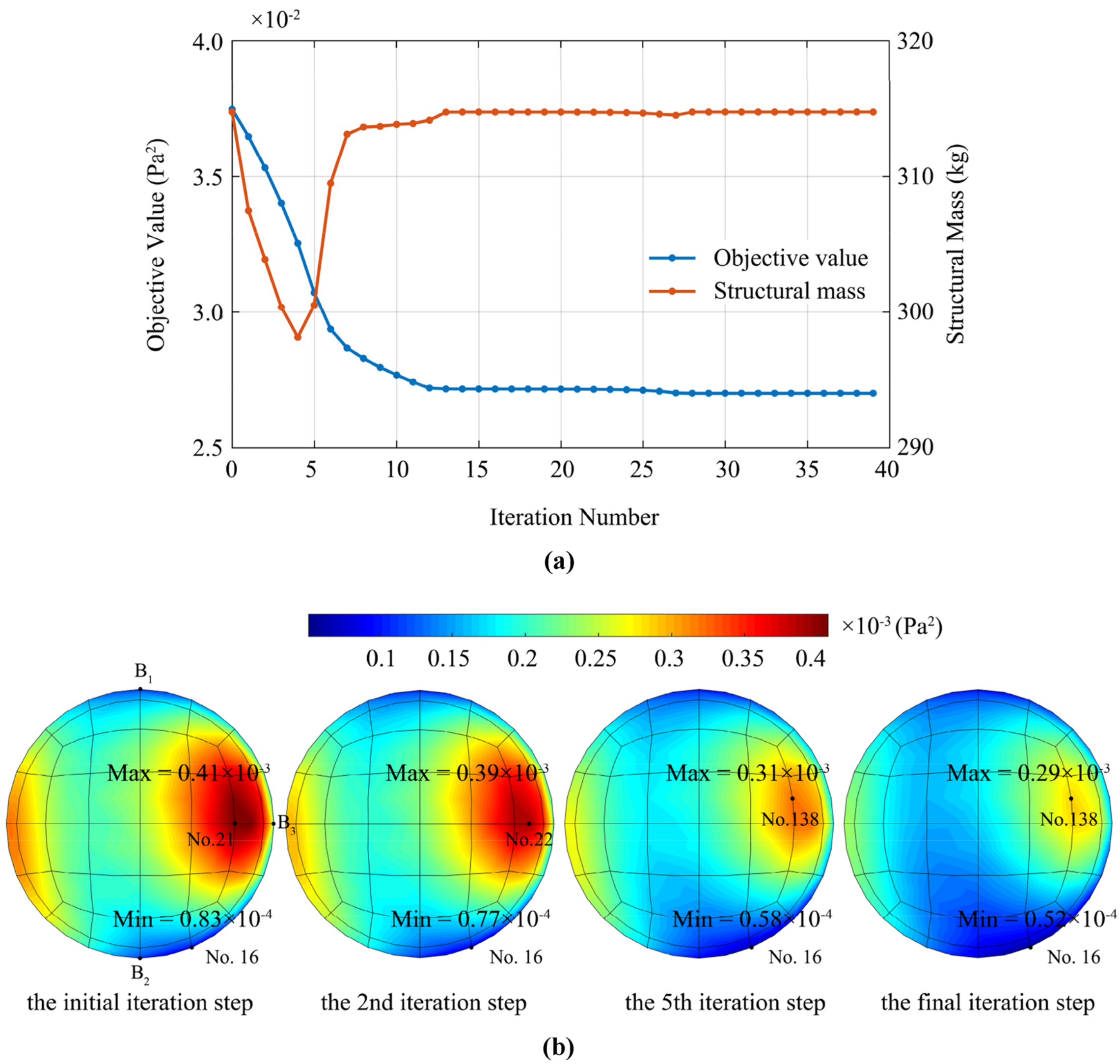

Fig. 16 Iteration history: **a** objective values and constraints, **b** nephograms at different iteration steps (bottom view)

to No. 22 in the 2nd iteration step and No. 138 in the 5th and the final iteration steps. In addition, the differences between the maximum and minimum values gradually decrease with the increase of the iteration number, which shows that the sound pressure distribution in the spatial domain is more uniform after optimization.

Figure 17a shows the comparisons between the initial and optimal objective curves in the time domain. Here, the longitudinal coordinate value is equal to the sum of the square of sound pressure on the hemisphere surface. In this example, the time when the sound pressure is received by the hemisphere surface for the first time is 0.008 s, and the longitudinal coordinate values are equal to zero before this time point. In addition, the longitudinal coordinate values suddenly increase at the time points about 0.013 s, 0.023 s, 0.034 s, and 0.044 s. The reason is that the transient force as shown in Fig. 14 changes significantly at these corresponding time points, and the sound spread time needs to be considered here. Moreover, we can also see that the optimal curve has a similar shape to the initial curve, but the values of former are smaller than those of latter. In addition, compared with the four initial peak values, the optimal peak values are decreased by 26.60%, 29.33%, 28.76%, and 29.81%, respectively, which means that the noise is more uniform and stable in the time domain.

Figure 17b shows the initial and optimal nephograms at different time points. At each time point, the optimal values are significantly smaller than the initial values. Moreover, compared with the maximum values of the four initial nephograms, the maximum values of the optimal nephograms are reduced by 12.02%, 24.82%, 22.50%, and 20.35%, respectively. Therefore, the above results show that

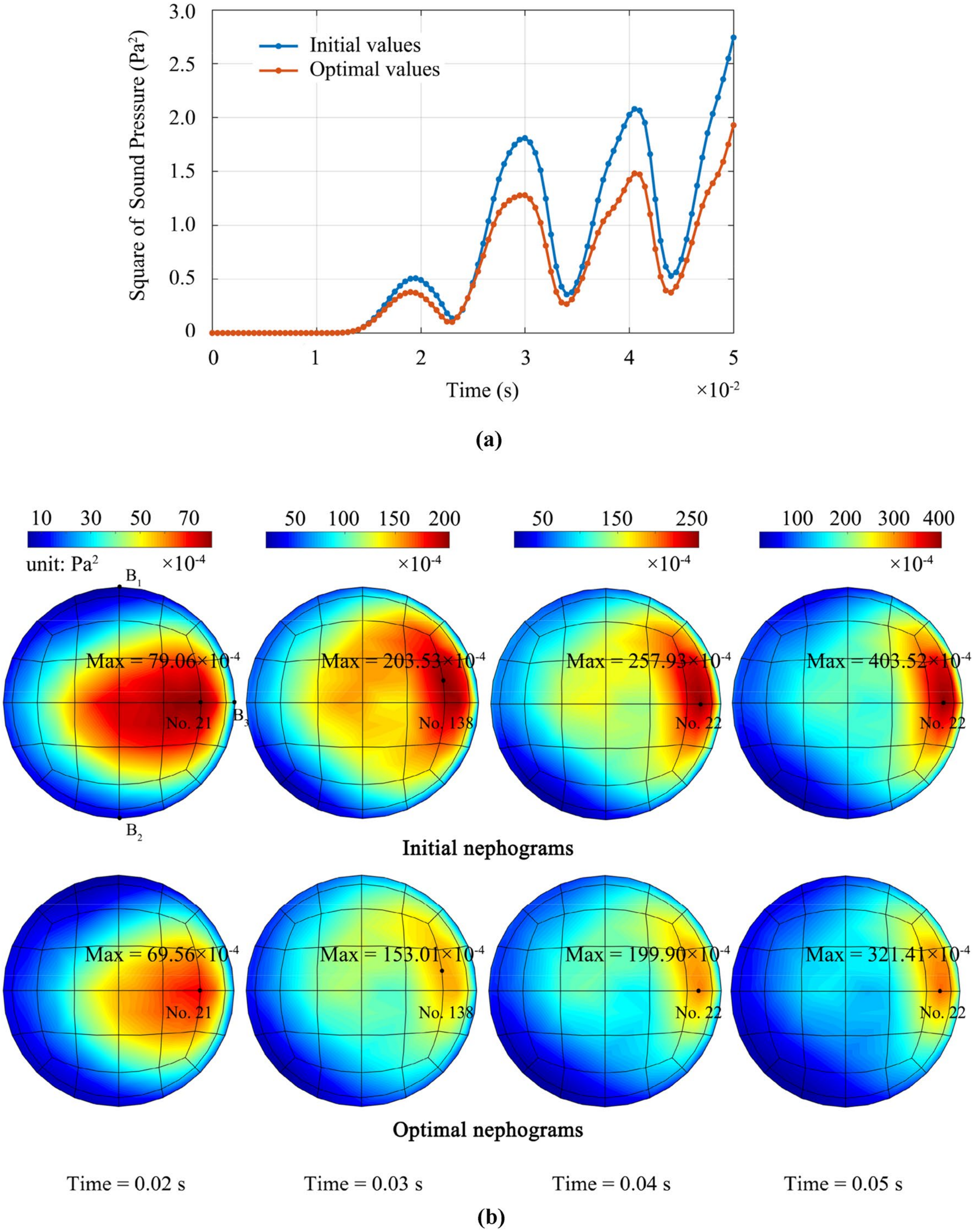

Fig. 17 Comparisons between the initial and optimal sound radiation: **a** objective value curves in the time domain, **b** nephograms at different time points

the time-domain sound radiation is successfully reduced by optimizing structural ply thicknesses, and the distributions of sound pressure are more uniform in both the spatial and time domains after optimization.

6.3 Computational performance for numerical examples

In this paper, both of the optimization examples are computed on a desktop PC with an Intel Core i7-6700 CPU and

32 GB memory. Similar to (Fallahi 2021), a hybrid programming approach is utilized in this paper. Specifically, the code of dynamic response calculation, sensitivity analysis and optimization algorithm is implemented in the self-programming MATLAB software, and the code of sound radiation analysis is written by FORTRAN.

In the example of the truncated cone structure, the number of degrees of freedom is 2316, and the numbers of iteration steps for Cases 1 to 4 are 35, 26, 33, and 40, respectively. In the example of the car model, the number of degrees of freedom is 2748, and the number of iteration steps is 40. Besides, for each example, the number of discrete time points in the time domain and the number of design variables are 101 and 9, respectively. The detailed computational time is given in Table 9.

7 Conclusions

In this paper, the undesired time-domain noise radiated from laminated curved shells under transient loads is successfully reduced by optimizing structural ply thicknesses. The optimization model is designed: the square of sound pressure on a prescribed reference surface in the sound medium or the structural surface over a period of time is chosen as the objective function; the structural ply thicknesses are taken as the design variables; and the structural mass is constrained. The FEM and Newmark integral method are employed to calculate the transient dynamic response, and a time-domain BEM is adopted to solve for the transient sound pressure. Moreover, the sensitivity formulation of transient sound pressure is obtained by directly differentiating response equations. Three numerical examples are presented to verify the accuracy of the sensitivity formulae and the effectiveness of the optimization model. The optimization results show that increasing the ply thicknesses near the loading positions can effectively reduce the time-domain sound radiation. Furthermore, the maximum nodal sound radiation in the spatial domain and the peak values in the time domain are all reduced after optimization, which indicates that the optimal sound radiation is more uniform and stable than the initial stage.

Appendix 1. Finite element equations for laminated curved shell elements

Figure 18 shows an eight-node curved shell element. In this figure, $(x{-}y{-}z)$ is the global coordinate system; $(x'{-}y'{-}z')$ is the local coordinate system; and $(\xi{-}\eta{-}\zeta)$ is the natural coordinate system with $-1 \le \xi, \zeta, \eta \le 1$. Here, we assume that $\mathbf{v}_{3i}$ is the nodal normal unit vector perpendicular to the middle surface of the element and that $\mathbf{v}_{1i}$ and $\mathbf{v}_{2i}$ are nodal unit vectors that are perpendicular to $\mathbf{v}_{3i}$ and orthogonal to each other. The displacement vector of any point within the element can be expressed in the following interpolation form:

$$\begin{Bmatrix} u \\ v \\ w \end{Bmatrix} = \sum_{i=1}^{8} N_i(\xi,\eta) \begin{Bmatrix} u_i \\ v_i \\ w_i \end{Bmatrix} + \sum_{i=1}^{8} \frac{T_i}{2} \zeta N_i(\xi,\eta) \begin{bmatrix} l_{1i} & -l_{2i} \\ m_{1i} & -m_{2i} \\ n_{1i} & -n_{2i} \end{bmatrix} \begin{Bmatrix} \alpha_i \\ \beta_i \end{Bmatrix} \tag{A1}$$

where the subscript i denotes the ith node; $\left(u_i\, v_i\, w_i\, \alpha_i\, \beta_i\right)^{\mathrm{T}}$ is the generalized nodal displacement vector; α_i and β_i are

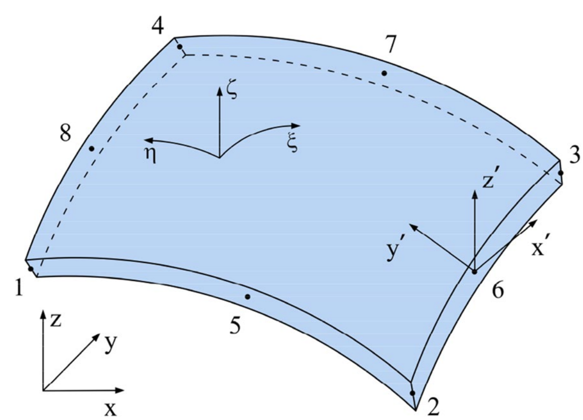

Fig. 18 Curved shell element

Table 9 Computational time for two numerical examples

	Time for transient dynamic response analysis (FEM) (s)	Time for transient sound radiation analysis (BEM) (s)	Time for sensitivity analysis per design variable (s)	Total time for the optimization process (h)
Truncated cone structure				
Case 1	25.65	38.41	30.39	3.30
Case 2	26.09	38.61	30.27	2.46
Case 3	25.67	37.79	30.00	3.09
Case 4	25.90	38.62	29.99	3.73
Car model	33.04	80.13	47.71	6.20

the rotation angles of $\mathbf{v}_{3i}$ around $\mathbf{v}_{2i}$ and $\mathbf{v}_{1i}$, respectively; N_i (Zhai et al. 2017) and T_i are the two-dimensional interpolation function and nodal thickness, respectively; and $(l_{ji}\, m_{ji}\, n_{ji})^{\mathrm{T}}$, with $j = 1, 2, 3$, are the direction cosines of $\mathbf{v}_{1i}$, $\mathbf{v}_{2i}$ and $\mathbf{v}_{3i}$, respectively. The stiffness matrix of the element can be written as:

$$\mathbf{K}^e = \int_{-1}^{1}\int_{-1}^{1}\int_{-1}^{1} \mathbf{B}^{\mathrm{T}}\mathbf{D}\mathbf{B}|\mathbf{J}|\, \mathrm{d}\xi \mathrm{d}\eta \mathrm{d}\zeta \tag{A2}$$

where $\mathbf{B}$ (Zhai et al. 2017) and $\mathbf{D}$ are the strain matrix and elastic matrix, respectively; and $\mathbf{J}$ is the Jacobian matrix:

$$\mathbf{J} = \sum_{i=1}^{8} \begin{bmatrix} N_{i,\xi}\left(x_i + \frac{\zeta T_i l_{3i}}{2}\right) & N_{i,\xi}\left(y_i + \frac{\zeta T_i m_{3i}}{2}\right) & N_{i,\xi}\left(z_i + \frac{\zeta T_i n_{3i}}{2}\right) \\ N_{i,\eta}\left(x_i + \frac{\zeta T_i l_{3i}}{2}\right) & N_{i,\eta}\left(y_i + \frac{\zeta T_i m_{3i}}{2}\right) & N_{i,\eta}\left(z_i + \frac{\zeta T_i n_{3i}}{2}\right) \\ \frac{N_i T_i l_{3i}}{2} & \frac{N_i T_i m_{3i}}{2} & \frac{N_i T_i n_{3i}}{2} \end{bmatrix} \tag{A3}$$

where the subscript i denotes the ith node; $(x_i\, y_i\, z_i)$ is the global nodal coordinate; and $N_{i,j}$, with $j = \xi, \eta, \zeta$, represent the derivatives of N_i with respect to the natural coordinates.

For an orthotropic shell, the material coordinate system is different from the global coordinate system due to the influence of the ply angle. Therefore, the elastic matrix $\mathbf{D}$ in the material coordinate system needs to be transformed into $\overline{\mathbf{D}}$ in the global coordinate system:

$$\overline{\mathbf{D}} = \mathbf{T}\mathbf{D}\mathbf{T}^{\mathrm{T}} \tag{A4}$$

with:

$$\mathbf{T} = \begin{bmatrix} \cos^2\theta & \sin^2\theta & 0 & 2\sin\theta\cos\theta & 0 & 0 \\ \sin^2\theta & \cos^2\theta & 0 & -2\sin\theta\cos\theta & 0 & 0 \\ 0 & 0 & 0 & 0 & 0 & 0 \\ -\sin\theta\cos\theta & \sin\theta\cos\theta & 0 & \cos^2\theta - \sin^2\theta & 0 & 0 \\ 0 & 0 & 0 & 0 & \cos\theta & -\sin\theta \\ 0 & 0 & 0 & 0 & \sin\theta & \cos\theta \end{bmatrix} \tag{A5}$$

in which θ is the ply angle.

As shown in Fig. 19, a laminated curved shell element consists of a stack of curved shell elements with different material properties and ply parameters. For such a laminated curved shell element, the elastic matrix is not a continuous function of the thickness coordinate ζ. Therefore, integration in the thickness direction is achieved by splitting the limits through each ply. In the calculation of the stiffness matrix of the kth ply, a new natural coordinate ζ^* with a value range of $[-1, 1]$ is introduced to replace the coordinate ζ. Thus, the stiffness matrix of the laminated element can be expressed by using the following superposition formula:

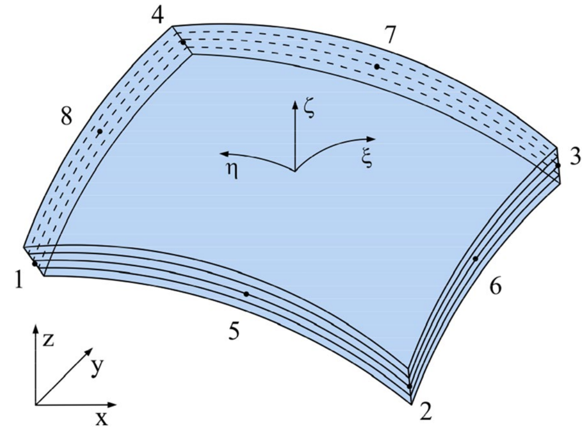

Fig. 19 Laminated curved shell element

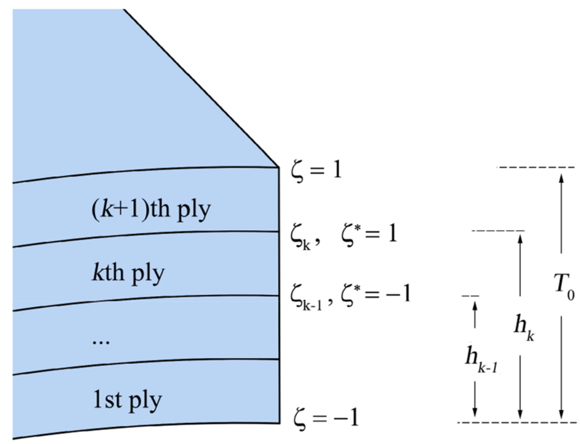

Fig. 20 Schematic diagram of coordinate transformation

$$\mathbf{K}^e = \sum_{k=1}^{\bar{k}} \int_{-1}^{1}\int_{-1}^{1}\int_{-1}^{1} \mathbf{B}_k^{\mathrm{T}}\overline{\mathbf{D}}_k\mathbf{B}_k|\mathbf{J}|_k|\mathbf{J}^*|_k \mathrm{d}\xi \mathrm{d}\eta \mathrm{d}\zeta^* \tag{A6}$$

where the subscript k denotes the kth ply; and $\bar{k}$ is the number of plies.

Figure 20 shows the relationships between different coordinates of the kth ply. For a laminated curved shell element with a total thickness of T_0, we can obtain the following relationships:

$$\begin{aligned} \zeta_{k-1} &= \frac{h_{k-1}}{T_0} \times 2 - 1 \\ \zeta_k &= \frac{h_k}{T_0} \times 2 - 1 \end{aligned} \tag{A7}$$

where h_{k-1} and h_k are the bottom surface height and top surface height of the kth ply, respectively; ζ_{k-1} and ζ_k represent the values of the two surfaces in the ζ coordinate. Therefore, the following relationship can be obtained:

$$\zeta = \frac{\zeta_k + \zeta_{k-1}}{2} + \frac{\zeta^*(\zeta_k - \zeta_{k-1})}{2} \tag{A8}$$

Combining Equations (A7) and (A8) yields:

$$\zeta = \frac{T_k}{T_0}\zeta^* + \left(\frac{2h_{k-1} + T_k}{T_0} - 1\right) \tag{A9}$$

where $T_k = h_k - h_{k-1}$ represents the thickness of the kth ply.

Here, we let $\omega_k = T_k/T_0$ and $\varphi_k = \left(2h_{k-1} + T_k\right)/T_0 - 1$. Thus, the expressions for $|\mathbf{J}^*|_k$, $\mathbf{J}_k$ and $\mathbf{B}_k$ in Equation (A6) are shown in Equations (A10) to (A13):

$$|\mathbf{J}^*|_k = \frac{\mathrm{d}\zeta}{\mathrm{d}\zeta^*} = \frac{T_k}{T_0} \tag{A10}$$

$$\mathbf{J}_k = \sum_{i=1}^{8}\begin{bmatrix} N_{i,\xi}\left[x_i + \frac{(\omega_k+\varphi_k\zeta^*)(T_k)_i l_{3i}}{2}\right] & N_{i,\xi}\left[y_i + \frac{(\omega_k+\varphi_k\zeta^*)(T_k)_i m_{3i}}{2}\right] & N_{i,\xi}\left[z_i + \frac{(\omega_k+\varphi_k\zeta^*)(T_k)_i n_{3i}}{2}\right] \\ N_{i,\eta}\left[x_i + \frac{(\omega_k+\varphi_k\zeta^*)(T_k)_i l_{3i}}{2}\right] & N_{i,\eta}\left[y_i + \frac{(\omega_k+\varphi_k\zeta^*)(T_k)_i m_{3i}}{2}\right] & N_{i,\eta}\left[z_i + \frac{(\omega_k+\varphi_k\zeta^*)(T_k)_i n_{3i}}{2}\right] \\ \frac{N_i\left(T_k\right)_i l_{3i}}{2} & \frac{N_i\left(T_k\right)_i m_{3i}}{2} & \frac{N_i\left(T_k\right)_i n_{3i}}{2} \end{bmatrix} \tag{A11}$$

$$\mathbf{B}_k = \mathbf{\Gamma}\begin{bmatrix} \mathbf{J}_k^{-1} & 0 & 0 \\ 0 & \mathbf{J}_k^{-1} & 0 \\ 0 & 0 & \mathbf{J}_k^{-1} \end{bmatrix}\sum_{i=1}^{8}\begin{bmatrix} N_{i,\xi} & 0 & 0 & \frac{-(\omega_k+\varphi_k\zeta^*)(T_k)_i N_{i,\xi} l_{2i}}{2} & \frac{(\omega_k+\varphi_k\zeta^*)(T_k)_i N_{i,\xi} l_{1i}}{2} \\ N_{i,\eta} & 0 & 0 & \frac{-(\omega_k+\varphi_k\zeta^*)(T_k)_i N_{i,\eta} l_{2i}}{2} & \frac{(\omega_k+\varphi_k\zeta^*)(T_k)_i N_{i,\eta} l_{1i}}{2} \\ 0 & 0 & 0 & \frac{-(T_k)_i N_i l_{2i}}{2} & \frac{(T_k)_i N_i l_{1i}}{2} \\ 0 & N_{i,\xi} & 0 & \frac{-(\omega_k+\varphi_k\zeta^*)(T_k)_i N_{i,\xi} m_{2i}}{2} & \frac{(\omega_k+\varphi_k\zeta^*)(T_k)_i N_{i,\xi} m_{1i}}{2} \\ 0 & N_{i,\eta} & 0 & \frac{-(\omega_k+\varphi_k\zeta^*)(T_k)_i N_{i,\eta} m_{2i}}{2} & \frac{(\omega_k+\varphi_k\zeta^*)(T_k)_i N_{i,\eta} m_{1i}}{2} \\ 0 & 0 & 0 & \frac{-(T_k)_i N_i m_{2i}}{2} & \frac{(T_k)_i N_i m_{1i}}{2} \\ 0 & 0 & N_{i,\xi} & \frac{-(\omega_k+\varphi_k\zeta^*)(T_k)_i N_{i,\xi} n_{2i}}{2} & \frac{(\omega_k+\varphi_k\zeta^*)(T_k)_i N_{i,\xi} n_{1i}}{2} \\ 0 & 0 & N_{i,\eta} & \frac{-(\omega_k+\varphi_k\zeta^*)(T_k)_i N_{i,\eta} n_{2i}}{2} & \frac{(\omega_k+\varphi_k\zeta^*)(T_k)_i N_{i,\eta} n_{1i}}{2} \\ 0 & 0 & 0 & \frac{-(T_k)_i N_i n_{2i}}{2} & \frac{(T_k)_i N_i n_{1i}}{2} \end{bmatrix} \tag{A12}$$

with

$$\mathbf{\Gamma} = \begin{bmatrix} 1 & 0 & 0 & 0 & 0 & 0 & 0 & 0 & 0 \\ 0 & 0 & 0 & 0 & 1 & 0 & 0 & 0 & 0 \\ 0 & 0 & 0 & 0 & 0 & 0 & 0 & 0 & 1 \\ 0 & 1 & 0 & 1 & 0 & 0 & 0 & 0 & 0 \\ 0 & 0 & 0 & 0 & 0 & 1 & 0 & 1 & 0 \\ 0 & 0 & 1 & 0 & 0 & 0 & 1 & 0 & 0 \end{bmatrix} \tag{A13}$$

Acknowledgements The research project is supported by the National Natural Science Foundation of China (U1508209, 11072049), Liaoning BaiQianWan Talents Program and Dalian Science and Technology Innovation Fund (2018J11CY003). The authors would like to acknowledge the support of these funds.

Data availability Not applicable.

Code availability The part of the code used during the current study are available from the corresponding author on reasonable request.

Declarations

Conflict of interest On behalf of all authors, the corresponding author states that there is no conflict of interest.

Replication of results The code and data are available from the corresponding author on reasonable request.

References

Adelman HM, Haftka RT (1986) Sensitivity analysis of discrete structural systems. AIAA J 24:823–832. https://doi.org/10.2514/3.48671

Assaad J, Decarpigny JN, Bruneel C, Bossut R, Hamonic B (1993) Application of the finite element method to two-dimensional radiation problems. J Acoust Soc Am 94:562–573. https://doi.org/10.1121/1.407069

Burnett DS (1994) A three-dimensional acoustic infinite element based on a prolate spheroidal multipole expansion. J Acoust Soc Am 96:2798–2816. https://doi.org/10.1121/1.411286

Chai YB, Gong ZX, Li W, Li TY, Zhang QF, Zou ZH, Sun YB (2018) Application of smoothed finite element method to two-dimensional exterior problems of acoustic radiation. Int J Comput Methods 15:1850029. https://doi.org/10.1142/S0219876218500299

Chen ZS, Waubke H, Kreuzer W (2008) A formulation of the fast multipole boundary element method (FMBEM) for acoustic radiation and scattering from three-dimensional structures. J Comput Acoust 16:303–320. https://doi.org/10.1142/S0218396X08003725

De Leon DM, de Souza CE, Fonseca JSO, da Silva RGA (2012) Aeroelastic tailoring using fiber orientation and topology optimization. Struct Multidisc Optim 46:663–677. https://doi.org/10.1007/s00158-012-0790-8

Denli H, Sun JQ (2007) Structural-acoustic optimization of sandwich structures with cellular cores for minimum sound radiation. J Sound Vib 301:93–105. https://doi.org/10.1016/j.jsv.2006.09.025

Du JB, Olhoff N (2007) Minimization of sound radiation from vibrating bi-material structures using topology optimization. Struct Multidisc Optim 33:305–321. https://doi.org/10.1007/s00158-006-0088-9

Du JB, Olhoff N (2010) Topological design of vibrating structures with respect to optimum sound pressure characteristics in a surrounding acoustic medium. Struct Multidisc Optim 42:43–54. https://doi.org/10.1007/s00158-009-0477-y

Du JB, Yang RZ (2015) Vibro-acoustic design of plate using bi-material microstructural topology optimization. J Mech Sci Technol 29:1413–1419. https://doi.org/10.1007/s12206-015-0312-x

Ebenezer DD, Stepanishen PR (1991) Wave-vector-time domain and Kirchhoff integral equation methods to determine the transient acoustic radiation loading on circular cylinders. J Acoust Soc Am 89:2532–2544. https://doi.org/10.1121/1.400693

Fallahi N (2021) GA optimization of variable angle tow composites in buckling and free vibration analysis through layerwise theory. Aerospace 8:376. https://doi.org/10.3390/aerospace8120376

Fernandez F, Tortorelli DA (2018) Semi-analytical sensitivity analysis for nonlinear transient problems. Struct Multidisc Optim 58:2387–2410. https://doi.org/10.1007/s00158-018-2096-y

Gill PE, Murray W, Saunders MA, Wright MH (1983) Computing forward-difference intervals for numerical optimization. Siam J Sci Stat Comput 4:310–321. https://doi.org/10.1137/0904025

Iott J, Haftka RT, Adelman HM (1985) Selecting step sizes in sensitivity analysis by finite differences. NASA Technical Memorandum 86382

Jeon JY, Okuma M (2008) An optimum embossment of rectangular section in panel to minimize noise power. J Vib Acoust 130:021012. https://doi.org/10.1115/1.2748456

Joshi P, Mulani SB, Gurav SP, Kapania RK (2010) Design optimization for minimum sound radiation from point-excited curvilinearly stiffened panel. J Aircraft 47:1100–1110. https://doi.org/10.2514/1.44778

Keulen FV, Haftka RT, Kim NH (2005) Review of options for structural design sensitivity analysis. Part 1: linear systems. Comput Method Appl Mech 194:3213–3243. https://doi.org/10.1016/j.cma.2005.02.002

Kim JK, Ih JG (2002) Prediction of sound level at high-frequency bands by means of a simplified boundary element method. J Acoust Soc Am 112:2645–2655. https://doi.org/10.1121/1.1517254

Lamancusa JS, Eschenauer HA (1994) Design optimization methods for rectangular panels with minimal sound radiation. AIAA J 32:472–479. https://doi.org/10.2514/3.12010

Lee TH (1999) An adjoint variable method for structural design sensitivity analysis of a distinct eigenvalue problem. J Mech Sci Technol 13:470–476. https://doi.org/10.1007/BF02947716

Lee KW, Park GJ (1997) Accuracy test of sensitivity analysis in the semi-analytic method with respect to configuration variables. Comput Struct 63:1139–1148. https://doi.org/10.1016/S0045-7949(96)00308-2

Li CX, Lian JJ (2020) Development and application of a pre-corrected fast Fourier transform accelerated multi-layer boundary element method for the simulation of shallow water acoustic propagation. Appl Sci 10:2393. https://doi.org/10.3390/app10072393

Li ZH, Zheng XQ (2017) Review of design optimization methods for turbomachinery aerodynamics. Prog Aerosp Sci 93:1–23. https://doi.org/10.1016/j.paerosci.2017.05.003

Liang X, Du JB (2019) Concurrent multi-scale and multi-material topological optimization of vibro-acoustic structures. Comput Method Appl Mech 349:117–148. https://doi.org/10.1016/j.cma.2019.02.010

Ma L, Cheng L (2019) Topological optimization of damping layout for minimized sound radiation of an acoustic black hole plate. J Sound Vib 458:349–364. https://doi.org/10.1016/j.jsv.2019.06.036

Mansur WJ (1983) A time-stepping technique to solve wave propagation problems using the boundary element method. Dissertation, University of Southampton

Martins JRRA, Hwang JT (2013) Review and unification of methods for computing derivatives of multidisciplinary computational models. AIAA J 51:2582–2599. https://doi.org/10.2514/1.J052184

Niu B, Olhoff N, Lund E, Cheng GD (2010) Discrete material optimization of vibrating laminated composite plates for minimum sound radiation. Int J Solids Struct 47:2097–2114. https://doi.org/10.1016/j.ijsolstr.2010.04.008

Ou DY, Mak CM (2011) The effects of elastic supports on the transient vibroacoustic response of a window caused by sonic booms. J Acoust Soc Am 130:783–790. https://doi.org/10.1121/1.3613696

Ou DY, Mak CM (2012) Transient vibration and sound radiation of a stiffened plate. J Vib Control 19:1378–1385. https://doi.org/10.1177/1077546312450731

Pereyra S, Lombera GA, Frontini G, Urquiza SA (2014) Sensitivity analysis and parameter estimation of heat transfer and material flow models in friction stir welding. Mater Res 17:397–404. https://doi.org/10.1590/S1516-14392013005000184

Qu YG, Zhang WM, Peng ZK, Meng G (2019a) Time-domain structural-acoustic analysis of composite plates subjected to moving dynamic loads. Compos Struct 208:574–584. https://doi.org/10.1016/j.compstruct.2018.09.103

Qu YG, Peng ZK, Zhang WM, Meng G (2019b) Nonlinear vibro-acoustic behaviors of coupled sandwich cylindrical shell and spring-mass-damper systems. Mech Syst Signal Process 124:254–274. https://doi.org/10.1016/j.ymssp.2019.01.048

Sharma N, Mahapatra TR, Panda SK, Hirwani CK (2018) Acoustic radiation and frequency response of higher-order shear deformable multilayered composite doubly curved shell panel: an experimental validation. Appl Acoust 133:38–51. https://doi.org/10.1016/j.apacoust.2017.12.013

Sharma N, Mahapatra TR, Panda SK (2019) Vibroacoustic analysis of thermo-elastic laminated composite sandwich curved panel: a higher-order FEM-BEM approach. Int J Mech Mater Des 15:271–289. https://doi.org/10.1007/s10999-018-9426-5

Taherifar R, Zareei SA, Bidgoli MR, Kolahchi R (2021) Application of differential quadrature and Newmark methods for dynamic response in pad concrete foundation covered by piezoelectric layer. J Comput Appl Math 382:113075. https://doi.org/10.1016/j.cam.2020.113075

Tian XH, Chen KA, Zhang YN, Wang L, Zhang J, Liu Y (2019) Modal expansion and spatial delay based fast transient structural sound radiation calculation. EPL 125:34001. https://doi.org/10.1209/0295-5075/125/34001

Tong Z, Zhang Y, Zhang Z, Hua H (2007) Dynamic behavior and sound transmission analysis of a fluid–structure coupled system using the direct-BEM/FEM. J Sound Vib 299:645–655. https://doi.org/10.1016/j.jsv.2006.06.063

Wang BP, Apte AP (2006) Complex variable method for eigensolution sensitivity analysis. AIAA J 44:2958–2961. https://doi.org/10.2514/1.19225

Wang YJ, Wang ZP, Xia ZH, Poh LH (2018) Structural design optimization using isogeometric analysis: a comprehensive review. Comput Model Eng Sci 117:455–507. https://doi.org/10.31614/cmes.2018.04603

Wu TW (2000) Boundary element acoustics: fundamentals and computer codes (advances in boundary elements). Southampton, UK

Yang XW, Li YM (2015) Structural topology optimization on sound radiation at resonance frequencies in thermal environments. Sci China Phys Mech 58:1–12. https://doi.org/10.1007/s11433-014-5539-5

Yang HS, Li HR, Zheng H (2016) A structural-acoustic optimization of two-dimensional sandwich plates with corrugated cores. J Vib Control 23:3007–3022. https://doi.org/10.1177/1077546315625558

Zhai JJ, Zhao GZ, Shang LY (2017) Integrated design optimization of structural size and control system of piezoelectric curved shells with respect to sound radiation. Struct Multidisc Optim 56:1287–1304. https://doi.org/10.1007/s00158-017-1721-5

Zhai JJ, Shang LY, Zhao GZ (2020) Simultaneous optimization of control parameters and placements of piezoelectric patches for active structural acoustic control of shell structures under random excitation. J Intel Mater Syst Struct 31:1204–1219. https://doi.org/10.1177/1045389X20916799

Zhang XP, Kang Z (2014) Dynamic topology optimization of piezoelectric structures with active control for reducing transient response. Comput Method Appl Mech 281:200–219. https://doi.org/10.1016/j.cma.2014.08.011

Zhang DD, Wang SW, Zheng L (2018) A comparative study on acoustic optimization and analysis of CLD/Plate in a cavity using ESO and GA. Shock Vib 2018:7146580. https://doi.org/10.1155/2018/7146580

Zhang L, Duan JX, Da LL, Xu GJ, Sun XH (2020) Vibroacoustic radiation and propagation properties of slender cylindrical shell in uniform shallow sea. Ocean Eng 195:106659. https://doi.org/10.1016/j.oceaneng.2019.106659

Zhao WC, Chen LL, Zheng CJ, Liu C, Chen HB (2017) Design of absorbing material distribution for sound barrier using topology optimization. Struct Multidisc Optim 56:315–329. https://doi.org/10.1007/s00158-017-1666-8

Zhao WC, Zheng CJ, Liu C, Chen HB (2018) Minimization of sound radiation in fully coupled structural-acoustic systems using FEM-BEM based topology optimization. Struct Multidisc Optim 58:115–128. https://doi.org/10.1007/s00158-017-1881-3

Zheng WG, Yang TL, Huang QB, He Z (2016) Topology optimization of PCLD on plates for minimizing sound radiation at low frequency resonance. Struct Multidisc Optim 53:1231–1242. https://doi.org/10.1007/s00158-015-1371-4

Zheng H, Zhang SQ, Zhao GZ (2021) Integrated design optimization of actuator layout and structural ply parameters for the dynamic shape control of piezoelectric laminated curved shell structures. Struct Multidisc Optim 63:2375–2398. https://doi.org/10.1007/s00158-020-02818-7

Zienkiewicz OC, Bando K, Bettess P, Emson C, Chiam TC (1985) Mapped infinite elements for exterior wave problems. Int J Numer Meth Eng 21:1229–1251. https://doi.org/10.1002/nme.1620210705